Vertical structure of clouds and precipitation during Arctic cold-air outbreaks and warm-air intrusions: observations from COMBLE

Christian P. Lackner[1], Bart Geerts[1], Timothy W. Juliano[2], Lulin Xue[2], and Branko Kosovic[2]

[1] University of Wyoming, Laramie, WY
[2] National Center for Atmospheric Research, Boulder, CO

Submitted to

J. Geophysical Research Atmosphere

Corresponding author: Bart Geerts, University of Wyoming, Atmospheric Science, 1000 East University Ave. Laramie, WY 82071. Email: geerts@uwyo.edu

Key Points

- Atmospheric profiling data collected at a coastal site at 69°N in Norway is investigated.
- Vertical velocity and cloud structure, and thus precipitation mechanisms, are fundamentally different in marine cold-air outbreaks vs. in warm-air intrusions.

Abstract

The Arctic is marked by deep intrusions of warm, moist air, alternating with outbreaks of cold air down to lower latitudes. The typical vertical structure of clouds and precipitation during these two synoptic weather extremes is examined at a coastal site at 69°N in Norway. The Norwegian Sea is a corridor for warm-air intrusions (WAIs) and frequently witnesses cold-air outbreaks (CAOs). This study uses data from profiling radar, lidar, and microwave radiometer, radiosondes and other probes that were collected during the Cold air Outbreaks in the Marine Boundary Layer Experiment (COMBLE) between 1 December 2019 and 31 May 2020. Marine CAOs are defined in terms of thermal instability relative to the sea surface temperature, and warm-air intrusions in terms of stratification of moist static energy between the surface and 850 hPa. Cloud structures in CAOs are convective, driven by strong surface heat fluxes over a long fetch of open water, with cloud tops between 2-4 km. The mostly open-cellular convection may contain substantial ice and produce intermittent moderate precipitation at the observational site, notwithstanding the low precipitable water vapor. In contrast, WAIs are marked by high values of precipitable water vapor and integrated vapor transport. WAI clouds are stratiform, with cloud tops often exceeding 6 km, sometimes layered, and generally producing persistent precipitation that can be heavier than in CAOs.

Plain Language Summary

The Arctic, more so than Antarctica, is marked by deep intrusions of warm, moist air, alternating with outbreaks of cold air down to lower latitudes. Here we examine the typical vertical structure of the updrafts, clouds and precipitation during these two weather types. We use data collected at a coastal site at 69°N in Norway during the Cold air Outbreaks in the Marine Boundary Layer Experiment (COMBLE). COMBLE ran between 1 December 2019 and 31 May 2020 with funding from the United States Department of Energy. The Norwegian Sea is a corridor for warm-air intrusions into the Arctic, and it frequently witnesses cold-air outbreaks, which in extreme events can be hazardous to maritime activities. The main findings of this study are: (1) the cold-air outbreak cloud regime is convective, driven by strong surface heat fluxes over a long fetch of open water. Clouds are rather low-topped yet they do produce precipitation. (2) Warm air intrusions are marked by much water vapor, high vapor transport, and deep, stratiform clouds generally producing persistent precipitation.

1. Introduction

The Arctic, more so than Antarctica, experiences frequent warm air intrusions (WAIs) deep into the Arctic interior, and frequently is the source of cold-air outbreaks (CAOs), especially in the cold season. In recent decades, the Arctic has been experiencing an amplified response to global warming: surface air temperatures have increased about three times as fast as the global mean in the past century (Serreze et al., 2009; Pithan & Mauritsen, 2014; Thoman et al., 2022). This amplified regional warming is expected to continue at least until the mid-21st century (Davy & Outten, 2020). As argued by Pithan et al. (2018) and Wendisch et al. (2021), a better understanding of how air masses are transformed on their way into and out of the Arctic is essential for improved prediction of weather and climate. This applies not just in the Arctic, but also in mid-latitudes, as these Arctic air mass intrusions and extrusions are an essential component of the mid-latitude baroclinic storm track.

The vertical structure and mesoscale organization of clouds and precipitation are an important component of this air mass transformation. These aspects are distinctly different in CAOs compared to WAIs (e.g., Ruiz-Donoso et al., 2020). A cold air mass originating over the Arctic ice (or boreal continents), flowing southward over open ocean water, typically transforms rapidly. Such event is evident as characteristic linear and cellular convective cloud structures in satellite imagery (Fig. 1a). Air-sea temperature differences can reach 30 K, especially just off the ice edge (Renfrew & Moore, 1999). This air-sea contrast, along with the strong surface winds, give rise to latent and sensible oceanic surface fluxes that are among the largest observed anywhere on Earth (Aemisegger et al., 2018). These fluxes result in shallow moist convection that deepens with fetch notwithstanding large-scale subsidence (e.g., Tornow et al., 2021). The intense air-sea heat exchange during boreal CAOs plays a key role in the transient subsidence of dense waters as part of the Atlantic meridional overturning circulation (Dickson et al., 1996). Marine CAOs are generally defined as anomalously cold periods with boundary layer thermal instability (Fletcher et al., 2016; Papritz & Grams 2018).

In contrast, Arctic WAIs (illustrated in Fig. 1b) are gradual, isentropically ascending synoptic pulses of poleward transport of moist static energy, commonly found over an intruding baroclinic zone (warm or occluded front). The terms “warm-and-moist intrusion”, “water vapor intrusion” or “moisture intrusion” are used as well (Doyle et al., 2011; Woods et al., 2013; Woods et al., 2017; You et al. 2022): typically, the poleward water vapor flux is coincident with

a poleward heat flux (Woods et al., 2017). Here we use the term WAI (as opposed to moist air intrusion) as a convenient contrast with CAO: essentially the WAIs, characterized by positive mid-tropospheric water vapor and temperature anomalies, represent the counterpart of CAOs, characterized by negative mid-tropospheric water vapor and temperature anomalies. WAIs are characterized by deep, stratified, moist southerly flow and may deposit large amounts of moisture, heat, and aerosol into the Arctic (Woods & Caballero, 2016), which may contribute to accelerated melting of the Greenland ice sheet (Oltmanns et al., 2019) and Arctic sea ice (Woods & Caballero, 2016; Yang & Magnusdottir, 2017). Due to the gradual isentropic ascent accompanying WAIs, deep, and sometimes multi-layered, clouds are typical. As a result, cloud and precipitation growth mechanisms are very different compared to CAOs.

CAOs commonly occur in the far northern Atlantic (Fletcher et al., 2016). WAIs are common in this region as well: the 70°N poleward moisture flux is far greater over the Norwegian Sea (~0° longitude) than at any other longitude (Woods et al., 2013).

The core objective of this study is to describe and contrast the vertical structure and organization of clouds and precipitation during CAO and WAI periods, at a coastal site in northern Norway, at 69.1°N.

Section 2 describes the data sources and analysis methods. Section 3 describes a CAO case and a WAI case. Composite structures during a 6-month period are described in Section 4. A discussion follows in Section 5, and the main findings are summarized in Section 6.

2. Data sources and analysis method

a. The COMBLE campaign

This study focuses on data collected by the first Atmospheric Radiation Measurement (ARM) Mobile Facility (AMF1) (Miller et al., 2016) between 1 December 2019 and 31 May 2020 at a small harbor (Nordmela) near Andenes on the island of Andøya in northern Norway (69.141 °N, 15.684 °E). The deployment of the AMF1 was part of a field campaign referred to as *Cold-air Outbreaks in the Marine Boundary Layer Experiment* (COMBLE) (Geerts et al., 2022). The site, some 1000-1300 km from the Arctic ice edge (Fig. 1), is an excellent location to study how air masses are transformed during marine CAOs. It is also along the main corridor for Arctic WAIs (Fig. 2 in Woods et al., 2013). As part of COMBLE, ARM instruments were

deployed also on the island of Bjørnøya, located at 75°N (Fig. 1), but these data are not used in this study.

The AMF1 deployment included scanning and profiling radars, lidars, passive microwave radiometers, an Atmospheric Emitted Radiance Interferometer (AERI), frequent radiosondes, radiation and surface flux sensors, and an aerosol observing system (Geerts et al., 2022). The most important instrument in this study is the sensitive narrow-beam 35 GHz (Ka-band) profiling radar known as KAZR, providing reflectivity, Doppler velocity, and Doppler spectral width. The ARM Data Archive products used in this study are summarized in Table 1. Several data products are multi-sensor value-added products, such as *ARSCLKAZRBND1KOLLIAS*, which contains cloud boundaries at a temporal resolution of 4 seconds and a vertical resolution of 30 meters, based on KAZR, micropulse lidar, and ceilometer data (Johnson et al., 2019). The *INTERPOLATEDSONDE* product linearly interpolates available radiosonde data on a fixed time-height grid with a 1-minute time resolution (Jensen et al., 2019).

Surface precipitation is estimated using four different gauges at the AMF1 site a tipping bucket rain gauge, an optical rain gauge, a Present Weather Detector (all part of the *MET* product), and a Pluvio-2 Weighing Bucket. Following a comparison of the different gauges under various weather conditions, and guidance from the "best estimate" product (*ARMBEATM*), we decided to use the Present Weather Detector in snow-dominated conditions (CAOs), since this gauge is the most reliable for snowfall, and the Pluvio-2 Weighing Bucket in rain (WAIs). Very low radiometer liquid water path (LWP) values, below a level of 30 g m^{-2}, are ignored due to the uncertainty of the statistical retrieval of LWP. Ice water path (IWP) is retrieved by vertically integrating IWC retrieved from KAZR in the *MICROBASEKAPLUS* product (Wang et al., 2019).

Other datasets used include the VIIRS satellite imagery from band I05 (11.45 micron) from the NOAA-20 and Suomi-NPP satellites at 375 m resolution, and gridded radar reflectivity data from the Norwegian meteorological service (Met Norway) at a spatial resolution of 1 km and temporal resolution of 5 min. The latter is based on a network of volume-scanning C-band (5 cm) radars, including the radar located on Trolltind Mountain approximately 17 km northeast of the AMF1 site (Saltikoff et al., 2017). We further use hourly European Centre for Medium-range Weather Forecasting (ECMWF) Reanalysis v5 (ERA5) (Hersbach et al., 2020) data for sea ice concentration, surface heat fluxes, and atmospheric variables during COMBLE. To determine

CAO conditions at Andenes, SST is inferred from the NOAA Optimum Interpolation 1/4 Degree Daily Sea Surface Temperature (OISST) Analysis, Version 2.1 (Reynolds et al., 2008). In order to determine the sources of airmasses advected over the AMF1 site, back trajectories are computed using HYSPLIT (Rolph et al., 2017) with hourly Global Forecast System (GFS) gridded model output at 0.25° resolution as input.

b. Definition of CAOs and WAIs

Periods when the AMF1 site experienced CAOs or WAIs are defined objectively, based on local lower-tropospheric conditions. Marine CAO periods are defined as M >0, surface (10 m) wind speed >5 m s^{-1}, and surface wind direction onshore (between 250° and 30° for the AMF1 site). Here, $M \equiv \theta_{SST} - \theta_{850\,hPa}$, where θ_{SST} is potential temperature evaluated with SST and sea level pressure, and $\theta_{850\,hPa}$ is evaluated at 850 hPa. M is a commonly used measure of thermal instability driven by ocean surface heat fluxes, although different upper reference levels have been used in the literature, between 900-700 hPa (e.g., Kolstad & Bracegirdle, 2008; Fletcher et al., 2016; West et al., 2019; Naud et al., 2020; Hu et al., 2022). The convective cloud layer is almost always deeper than the 850 hPa level at Andenes during CAOs (Geerts et al., 2022), so this upper reference level is generally within the mixed layer.

Large-scale circulation studies define WAIs in terms of the vertically-integrated or fixed-level (e.g., 850 hPa) poleward moisture or heat flux (e.g., You et al. 2022). At the location of Andenes, close to a very strong climatological SST anomaly above the zonal mean, WAI periods can be defined based on two conditions: $S \equiv \theta_{e,850hPa} - \theta_{e,surface} > 0$ and the average wind speed between the surface and 850 hPa exceeds 5 m s^{-1} from the SSW (along-shore direction). The orientation SSW (more specifically, 210°) is chosen, rather than southerly, based on the orientation of the Norwegian coastline in the study region, because WAIs are often channeled along the coastline (e.g., Kim et al. 2017). The S-parameter is defined in terms of equivalent potential temperature θ_e because WAIs are marked by elevated moisture and warmth. $\theta_{e,surface}$ refers to the surface (2 m) air, not the SST. The mean cold-season surface air θ_e along the northern Norwegian coast is highly anomalous for its latitude (compared to other places at the same latitude), and we found that it is sufficient to require that θ_e is even higher at 850 hPa (S > 0). We did not examine the applicability of this simple definition to other high-latitude oceans.

Pithan et al. (2018) also use an upper reference level of 850 hPa (~1.5 km) for their definition of WAIs.

To compute *M* and *S* values, we use 850 hPa wind, temperature and moisture from the AMF1 *INTERPOLATEDSONDE* product (Table 1). Sea level pressure, surface (2 m) temperature and humidity, and surface (10 m) wind are obtained from the *MET* product or, if this is not available, the *MAWS* product (Table 1). (*MET* and *MAWS* meteorological data generally agree very well.) Finally, SST just offshore the AMF1 site is retrieved from the daily NOAA OISST data. For all variables, a 3-hour running mean is used to determine the CAO/WAI periods, and a minimum duration of 3 hours is required for a CAO or WAI event to occur. Additionally, gaps of less than 3 hours between two consecutive events are bridged regardless of conditions during the gap. The precise start and end times of the CAO periods at the AMF1 site are listed in Table S6 in the Supplement to Geerts et al. (2022). ERA5-based composite analyses of CAOs and WAIs use the nearest hour for the start and end times.

The resulting WAI and CAO periods at Andenes during COMBLE are shown in Fig. 2. According to these definitions, CAO (WAI) conditions prevailed at Andenes during 18.7% (17.4%) of the time during the COMBLE field phase (1 Dec 2019 – 31 May 2020). Therefore, *CAO and WAI conditions (as defined herein) are about equally common, and represent only the tail ends of synoptic variability*. Durations of CAO and WAI conditions are similarly distributed (Fig. 2), controlled by synoptic time scales. The median date of occurrence of CAOs fell on 13 March 2020, and that of WAIs fell on 08 February 2020. Reanalysis-based climatologies show that CAOs are most common in the cold season over the far northern Atlantic Ocean (Fletcher et al., 2016; Mateling 2022). The seasonal contrast probably is smaller for WAIs, but their impact is most pronounced in winter (Woods & Caballero, 2016).

3. Example CAO and WAI cases during COMBLE

a. A CAO example

One of the more intense CAOs during COMBLE occurred on 13-14 March 2020 (Fig. 1a). Specifically, this CAO started at 01:18 UTC 13 Mar and ended at 04:53 UTC 14 Mar 2020 at Andenes, according to our CAO criteria (Section 2b). During this period, the observed mean *M* value at Andenes was 8.4 K, making it the most intense CAO event at the AMF1 site during COMBLE. The mean surface air temperature was -3.2°C, while the offshore SST was 5.4°C. A

persistent wind averaging 10.1 m s^{-1} blew, mainly from the NNW. GFS-based 36-hour back-trajectories (Fig. 3) reveal that air at lower levels (1 km and 2 km above MSL) flows from the central Arctic through the Fram Strait, west of Svalbard, and directly to Andenes. At higher levels (3.5 km above MSL), the air originates slightly further east in the Arctic and moves closer to Svalbard. This CAO was the second most intense event in the Fram Strait in the month of March between 1979 and 2020, according to ERA5 data (Dahlke et al., 2022). The intensity of the event is Evident in the strong ERA5 850 hPa temperature anomalies compared to the 1991-2020 March mean. They reach from -7 K between Andoya and Bear Island to -14 K in the Fram Strait, and even stronger anomalies occurred above the sea ice (Fig. 4e). ERA5 surface sensible heat fluxes during this event peaked around 770 W m^{-2} in the Fram Strait, decreasing to 110 W m^{-2} just north of Andenes (Fig. 4a). The surface latent heat flux along the trajectory was slightly more steady with fetch, decreasing from 350 W m^{-2} in the Fram Strait to 120 W m^{-2} just north of Andenes. These large heat fluxes deepen, moisten, and warm the convective boundary layer via convective and turbulent exchanges, and are responsible for the rapid air mass modification evident in the steady Lagrangian increase of θ_e at 850 hPa (Fig. 4c). Lagrangian back trajectories from Andenes during this CAO show some slight subsidence at low to mid-levels (Fig. 3). The intense evaporation (Fig. 4a) and rather high precipitation rate (Fig. 4e) in marine CAOs implies rapid cycling of atmospheric water vapor, which has been estimated to have a typical residence time of about 1 day (Papritz & Sodemann, 2018), i.e. an order of magnitude shorter than the global mean.

Satellite images, such as the one shown in Fig. 1a, show shallow linear convection (cloud streets) in the first ~500 km from the ice edge, deepening with fetch and transitioning to even deeper open-cellular convection closer to Andenes. The skew-T log-p profile at Andenes around the same time (Fig. 5a) shows a super-adiabatic surface layer, high low-level relative humidity, a low lifting condensation level (LCL), and a deep well-mixed convective layer, with a temperature profile close to moist adiabatic up to ~540 hPa (~5.0 km). A capping inversion is absent in this case, and weak stratification continues up to the tropopause at 475 hPa, implying little inhibition for convective overshooting and little dynamic support for anvil spreading. The air is moist but not saturated (with respect to liquid water) in this sounding (Fig. 5a), but other nearby soundings show saturated layers (not shown). There is very little wind shear in the ~5 km deep well-mixed layer (Fig. 5a). Surface-based Convective Available Potential Energy (CAPE)

during this CAO was small (220 J kg^{-1} in Fig. 5a) and variable from sounding to sounding, depending on the balloon ascent path relative to the convective showers. Yet SST-based CAPE during this CAO exceeded 1000 J kg^{-1} just offshore Andenes, for all soundings during this CAO (nearly 1400 J kg^{-1} at 11:26 UTC, Fig. 5a).

Profiling radar time-height transects, such as the one shown in Fig. 6, show isolated convective cells topping at 5 km, with some shallower interspersed cells (Fig. 6a). Some of these cells (such as the one around 11:20 UTC, labeled cell 'A' in Fig. 6a) are marked by updrafts strong enough to loft hydrometeors (Fig. 6b), large values of spectral width (Fig. 6c), high LWP occasionally exceeding 1000 g m^{-2} (1 mm) (Fig. 6d), and IWP values that are rather extreme even for CAOs, as will be shown below (Fig. 6d). Yet other cells appear to be in a decaying phase, without updrafts, low spectral width, no liquid water, and a bottom-heavy vertical distribution of hydrometeors, such as the cell at 10:45 UTC (cell B). According to the KAZR profiles, most cells produce surface precipitation (Fig. 6a), but the Present Weather Detector registered little precipitation during cell A and moderate snowfall (0.7 mm liquid equivalent in around 20 minutes) during cell B (Fig. 6e). The precipitation phase (snow) is assumed based on the below-freezing surface temperature. This question is revisited later. A high Doppler spectral width can be due to either a diversity of fallspeeds within the radar gate, as is common for rain of different sizes. In regions dominated by snow particles, a larger spectral width is more commonly due to atmospheric turbulence in the inertial subrange (e.g., Aikins et al. 2016). Here, high spectral width values coincide with increased LWP values as well as strong vertical hydrometeor motions. Thus, high spectral width values likely have contributions from the variability of hydrometeors in mixed-phase clouds and turbulence. Both along the coast and offshore, the ERA5 cumulative precipitation from these convective cells is significant (Fig. 4e). However, surface precipitation rate estimation in marine CAOs is rather uncertain, given that these relatively small cells challenge precipitation retrievals using spaceborne passive microwave or radar data (e.g., Milani et al., 2021). Furthermore, numerical weather prediction models, such as ECMWF, are challenged as well since these convective cells are parameterized, not resolved.

For this CAO, the ERA5 precipitation slightly exceeded the gauge estimate (from the Present Weather Detector) at the AMF1 site, although for all CAOs in COMBLE combined, ERA5 and gauge values agree very well (Table 2). Note that surface precipitation at the AMF1

site may have an orographic component given the strong onshore flow during CAOs. This is less likely during WAIs, since the low-level flow is generally along the Norwegian coast.

Surface precipitation type was difficult to identify with the AMF1 measurements (Mages et al., 2022). The surface temperature remained below freezing during this CAO. The high MPL depolarization ratio (not shown) indicates that the hydrometeors mostly are snow particles, possibly with some embedded pockets of graupel; however, such pockets are difficult to identify. A Parsivel disdrometer was deployed as part of the AMF1 instrument suite; while it provides fallspeed distributions, in strong winds, turbulence results in a broad scatter of estimated fallspeeds, so it is difficult to identify periods with graupel fall.

Frequency-by-altitude diagrams of KAZR reflectivity, Doppler velocity (i.e. hydrometeor vertical motion) and Doppler spectral widths for this CAO are shown in Fig. 7. The precipitation profiles are highly heterogenous: ~10 % of the profiles have reflectivity values over 15 dBZ up to levels close to the cloud top, and the most common cloud tops are at 3.0-4.5 km MSL (Fig. 7a). Note that Ka-band (35 Ghz) reflectivity "saturates" in the 20-25 dBZ range, since under heavy snowfall the dominant scatterers fall in the Mie regime (e.g., Grasmick et al., 2022), i.e. the KAZR reflectivity cannot be used to distinguish snowfall intensity or hydrometeor size in the upper end of the reflectivity spectrum in Fig. 7a.

Depending on the altitude, hydrometeors are lofted in 15-35% of the profiles, especially near cloud top (Fig. 7c). Only 3-5% of the hydrometeors are lofted fast (at over 1 m s^{-1}), and only 1-3% fall at 3 m s^{-1} or more, indicating that strong vertical drafts (up or down) and heavily rimed snow (graupel with a substantial fallspeed) are relatively rare. Mages et al. (2022) retrieve air vertical velocity and report updrafts ranging between 2-8 m s^{-1} in 13 CAOs in COMBLE, including the 13-14 March 2020 event. The distribution of spectral width values is rather broad, with 10% of the profiles having a spectral width over 0.6 m s^{-1} (Fig. 7e); these high values are encountered at all levels in cloud.

b. A WAI example

One of the more intense and long-lived WAIs in COMBLE started at 01:47 UTC 3 Dec and ended at 02:14 UTC 5 Dec 2019 at Andenes (Fig. 2). The mean *S* value at Andenes during this event was 5.1 K, the mean 2-m temperature was 5.9 °C, and 10-m wind averaged 6.5 m s^{-1} from the SW (216 °), i.e. along-shore. The large poleward transport of heat and moisture in this

WAI was associated with an occluded frontal system with a surface low just northeast of Iceland (collocated with the comma cloud in the lower left of Fig. 1b), and a strong southwesterly low-level jet off Scandinavia. Air during this WAI originated in the northeast Atlantic (southwest of Ireland) and moved entirely over the ocean (Fig. 3). Commonly used parameters depicting WAIs are the vertically-integrated specific humidity, referred to as precipitable water vapor (PWV, units mm or kg m^{-2}), and the vertically-integrated water vapor transport (IVT, kg m^{-1} s^{-1}) (e.g., Doyle et al., 2011; Fan et al., 2022). As a reference, commonly used threshold IPV values for an *atmospheric river* (mainly a mid-latitude phenomenon) are in the 100-250 kg m^{-1} s^{-1} range. More specifically, atmospheric rivers are defined based on a threshold IVT that is a percentile (e.g., the 85th percentile) of the geographically and seasonally specific IVT distribution, with a fixed lower limit of 100 kg m^{-1} s^{-1} (e.g., Guan & Waliser, 2015; Ralph et al., 2017; Rutz et al., 2020). A plume of high PW, high 850 hPa θ_e, and high IVT values can be seen off Scandinavia during this WAI (Fig. 4d). These three variables are considerably higher over the Norwegian Sea during the WAI than the CAO (Fig. 4c) because of the higher lower-tropospheric temperature (Fig. 4e and f) and thus a higher saturation vapor pressure. This plume wraps around the low to the west (Fig. 4d), but the system travels further east towards northern Scandinavia over the next two days (not shown).

The Andenes sounding during this WAI (Fig. 5b) reveals deep moisture, stratified conditions (with several jumps in θ_e below 500 hPa), no CAPE relative to the SST, and a southwesterly low-level jet with a wind speed of 26 m s^{-1} at 850 hPa. At 700 hPa, the relative humidity is about the same as during the CAO (Fig. 5a), at or near saturation, but the 700 hPa temperature is 22 K higher (nearly twice as large as the temperature difference at the surface), implying much water vapor aloft. The IVT value, 401 kg m^{-1} s^{-1} (Fig. 5b), exceeds the 99th percentile for the month of December 2019, indicative of an atmospheric river. Values for PWV (18.2 kg m^{-2}) and 850 hPa θ_e (301 K) in this sounding are also exceptionally high for this latitude. The IVT value was only exceeded during one other WAI event in early January 2020, and the PWV was only exceeded during a WAI event in late May 2020. Surface sensible and latent heat fluxes are negligible or even negative within the atmospheric river (Fig. 4b), and heavy precipitation falls along the Scandinavian coast and along the baroclinic northern edge of this comma head (Fig. 4f).

The clouds and precipitation at the AMF1 site are the result of widespread stratified ascent. Lagrangian back trajectories show air parcels generally ascending for at least 12 hours (since 00 UTC on 4 Dec 2019) (Fig. 3). Yet hydrometeors seen by radar generally descend from cloud top (Fig. 8b), growing in size towards the surface (Fig. 8a), as is typical for stratiform precipitation. Compared to the convective cells shown in Fig. 6, the vertical velocities are weak and the Doppler spectral width values are small (above the freezing level). Snow transitions to rain just below the freezing level (near 850 hPa or 1 km MSL), resulting in a large fallspeed and high spectral width. Radiometer LWP estimates are mostly uncertain (liquid accumulation on the instrument), but reliable LWP estimates are quite high, exceeding 1000 g m^{-2} (Fig. 8d), due to water below the freezing level, and possibly supercooled liquid aloft. Compared to the CAO case, IWP values are lower (Fig. 8d). The reflectivity transect (Fig. 8a) reveals several plumes or streaks of falling and growing snow particles, mostly emerging between the -10 and -20°C isotherms. In this particular transect, a sloping dry layer is present between 11-14 UTC, and ice particles from the cirrus layer appear to be feeding the shallow cloud layer (tops around -10°C), contributing to bursts of higher IWP (Fig. 8d) and heavier precipitation on the ground (Fig. 8a). On average, the precipitation rate at Andenes during this WAI is significantly higher than the rate during the CAO examined in Section 3a, according to both observations and ERA5 (Table 2). The gauge precipitation rate (from the Pluvio-2 weighing bucket) exceeded the ERA5 precipitation rate for this WAI, but for all WAIs combined, ERA5 and gauge again agree very well (Table 2).

The distribution of reflectivity and hydrometeor vertical velocity above the melting layer (which typically falls in the 1.0-1.5 km MSL layer, according to Fig. 7b, d, and f) are narrower in this WAI than in the CAO (Fig. 7), indicating rather homogenous stratiform precipitation. Spectral width values in the snow layer are small, indicating little turbulence. Reflectivity increases steadily between the echo tops and ~3 km MSL, and the average downward Doppler velocity (a good estimate of the mean fallspeed of the larger hydrometeors) increases from 0.5 to ~1.0 m s^{-1}. The large spectral width and diverse Doppler velocities below the freezing level are a reflection of the diversity of rain drop sizes.

4. Composite CAO and WAI structures

a. Environmental and cloud conditions

364 The average surface sensible and latent heat fluxes during all Andenes-centered CAOs
365 and WAIs during COMBLE (Fig. 2) is shown in Fig. 9a. The sensible heat flux peaks at 290 W
366 m^{-2} in the Fram Strait and decreases rapidly and then more gradually with fetch from the ice edge
367 during CAOs. Just north of Andenes, the average sensible heat flux is 120 W m^{-2}. The latent heat
368 flux is more uniform across the Norwegian Sea during CAOs, ranging from 120-170 W m^{-2}.
369 Heat fluxes tend to be small during WAIs (Fig. 9b). For the Andenes-centered WAIs, the
370 sensible heat flux is positive to the north as the pre-WAI flow is generally from the cold northern
371 European land area (Fig. 9b).
372 On the other hand, both PWV and IVT are significantly higher during WAIs than during
373 CAOs (Fig. 9c and d). During CAOs, 850 hPa θ_e, PWV and IVT values grow steadily from the
374 ice edge towards the Scandinavian coast (Fig. 9c), evidence of the surface-driven air mass
375 transformation of the deepening marine BL. The poleward decrease in 850 hPa θ_e in WAIs north
376 of Andenes should be seen mainly as a baroclinic zone with poleward isentropic ascent (Fig. 9d).
377 The andenes-centric WAI composite structure shown in Fig. 9 evolves over time: θ_e, PWV,
378 temperature anomalies and the precipitation field tend to move northeastward in the following
379 12-24 hours, although little warming, moistening, and surface precipitation occur poleward of
380 the sea ice edge over this time period except off the east coast of Greenland. After 24 hours, the
381 WAI conditions start to rapidly weaken over the whole study area. This assessment is based on
382 composite charts identical to Fig. 9, but for time periods that lag the Andenes-centric WAI
383 periods by 6-36 hours (not shown).
384 The average precipitation rate during WAI periods only slightly exceeds that during CAO
385 periods both along the Norwegian coast, over the Norwegian Sea (Fig. 9e and f), and at Andenes
386 (Table 2). For both WAI and CAO composites, the observed precipitation rate at Andenes
387 closely matches the ERA5 estimate. This by itself is an interesting finding, and should be further
388 corroborated with other data, e.g. the network of precipitation gauges along the Norwegian coast.
389 Terrain-related variations in precipitation may exist at scales too fine for ERA5 or other
390 reanalyses to capture (e.g., Minder et al. 2008). Simulated precipitation rates in CAOs over open
391 water are poorly constrained for lack of offshore observations.
392 *ERA5 data indicate that the CAO cloud regime is a significant source of precipitation*.
393 This is confirmed by spaceborne radar-based estimates of convective snowfall rate over the
394 Norwegian Sea (Kulie et al., 2016, 2018). In contrast to the slight differences in average

precipitation rate over the open ocean and at the coast (between WAI and CAO), precipitation differs substantially over the Arctic sea ice. CAOs produce virtually no precipitation over the Arctic sea ice (including east of Greenland); some snowfall occurs east of Svalbard were the sea ice fraction was variable during COMBLE and a broad marginal ice zone prevailed; but almost all precipitation occurs equatorward of the average sea ice edge (Fig. 9c). WAIs, on the other hand, can produce more precipitation over the ice especially along the southeastern coast of Greenland (Fig. 9d). Of note is also the poleward retreat of the sea ice edge during WAIs compared to CAOs (Fig. 9a,b). The different distribution of CAO and WAI events throughout the 6-month study period, as well as increased melting during WAIs, are likely both contributing factors. On the one hand, the last week of May 2020 was exceptionally warm at Andenes with a series of WAI events (Fig. 2). This anomalous event likely contributes to the lower average sea ice extent during WAIs due to how late in the season it was. If Fig. 9 is created with time periods that precede Andenes-centric time periods by 48 hours, sea ice extent is noticeably larger in some areas (not shown), indicating that during the identified WAIs sea ice retreats poleward.

We now examine distributions of cloud and environmental parameters during all CAOs and WAIs during COMBLE (Fig. 10). Small *S* values dominate during WAIs, with higher values becoming rapidly less common (Fig. 10a). The WAI periods are part of a broader distribution in which the lower troposphere is often potentially unstable over Andenes in the cold season ($\theta_{e,850mb} < \theta_{e,surface}$), i.e. negative *S* values. On the other hand, *M* values during CAOs have a well-defined peak (or multiple peaks) well above zero: winds from the north or west typically are associated with sizable thermal instability over the warm Gulf Stream waters off Andenes. On average, CAOs are only 4 K colder than WAIs at the surface, and both conditions occur under a broad temperature range (Fig. 10b). Surface air temperature is almost always above freezing during WAIs, but is below freezing during CAOs for 35% of the time.

WAIs generally have higher PWV and IVT than CAOs (Fig. 10j and k). The IVT during CAOs typically is less than half of the WAI IVT, but can be important as the result of >1000 km span of strong surface latent heat fluxes over the northern seas (Fig. 9a). IVT values exceeding 200 kg m^{-1} s^{-1} are not uncommon during WAIs (Fig. 10k). Water vapor generally is advected from the southwest during WAIs, and from the northwest during CAOs (Fig. 10l).

The highest LWP (Fig. 10h) values are encountered during WAIs. Radiometer LWP is undersampled during WAIs, since this field often is rain-flagged (as is the case in Fig. 8d), on

account of drops on the reflector surface, which contaminate the LWP estimate. This rarely affects CAO clouds, because snowfall is more common. Therefore, the LWP estimates during WAIs mostly refer to periods of non-precipitating clouds, but during CAOs they include most clouds. In CAOs, the LWP is almost all supercooled liquid, whereas in WAIs, much of the liquid in the column occurs below the freezing level. Radar retrieved IWP values above 1.5 kg m^{-2} are almost exclusively found in CAOs (Fig. 10i). The largest IWP values during CAOs can exceed 4 kg m^{-2} for the deepest open cellular clouds, as shown in Fig. 6d. During WAIs, IWP values from 0.2-0.7 kg m^{-2} are more frequent than during CAOs, indicating that presence of snow above the freezing level is common in WAIs.

Moderate precipitation rates exceeding 1 mm hr^{-1} are more frequent during WAIs (Fig. 10g). This is in agreement with Mateling et al. (2022), who contrast precipitation rates during CAOs (defined as in this study) against non-CAO periods in the Norwegian Sea. They find heavy (light) snowfall rates to be less (more) common during CAOs, compared to non-CAOs, in the December through May period.

Cloud vertical extent (Fig. 10d-f) is derived from instantaneous radar/lidar profiles at a time resolution of 4 second. Therefore, the distribution of cloud vertical extent in Fig. 10d-f includes both variation between events, and variation within individual cloud elements. In WAIs, cloud bases and tops are rather uniform, but a single cumulus cloud during a CAO can have a range of cloud base and especially cloud top heights, as evident from the illustration in Fig. 6a. Cloud top temperature (Fig. 10c) is inferred from cloud top height (Fig. 10d) using *INTERPOLATEDSONDE* data. The cloud tops refer to the height of the first KAZR echo top, and the cloud depth (Fig. 10f) is measured from cloud base to this cloud top.

WAIs include both shallow clouds that may produce light drizzle (warm-rain processes), and very deep stratiform clouds with tops below -40°C (Fig. 10d and c). CAO clouds typically are more shallow: clouds as deep as in the intense CAO on 13 March (Fig. 6) are very rare (Fig. 10f). The deepest CAO clouds (>5 km) are due not to more intense CAO conditions, but rather some brief instances of a stratiform cloud layer above the cumulus convection, e.g. on account of an approaching frontal system. Cloud layering is rather common during WAIs, as is the case in the WAI example in Fig. 8: the composite KAZR reflectivity profile analysis indicates that two cloud layers are present in 31% of all WAI profiles, and three or more cloud layers in 17% of them (Table 3). Layering is present in CAOs as well, but it is less common (Table 3) and can

457 occur due to the presence of an elevated cloud layer or a convective anvil stretching over nearby
458 more shallow cumulus clouds. Clear sky conditions are rare during either phenomena.
459 Composite profiles of the median potential temperature, θ, specific humidity q, and θ_e
460 (Fig. 11) during CAOs are distinctly different from those during CAOs. The difference between
461 the two populations is largest not at the surface but rather between 1-3 km MSL, which is not
462 surprising given the coastal location. In CAOs, θ_e is close to constant with height in the lowest 3
463 km, whereas it steadily rises in WAIs. This is fundamental to the observed difference in cloud
464 structure. Low-level meridional moisture advection is almost exclusively positive/southerly
465 (negative/northerly) during WAIs (CAOs) (Fig. 11e). The magnitude of the moisture advection
466 peaks near the surface during CAOs (because of strong low-level winds and an adiabatic lapse
467 rate) and peaks near 1 km MSL during WAIs (because of the low level jet and stratified lapse
468 rate) (Fig. 11f).
469
470 *b. Vertical structure of cloud and precipitation*
471 Frequency-by-altitude diagrams matching Fig. 7, but for all CAO and WAI periods, are
472 shown in Fig. 12. CAOs are mostly far shallower than the intense 13 March 2020 event: a
473 distinct drop-off in frequencies is found around 2 km MSL (Fig. 12a). Few echoes are found
474 above 5 km. Heavy snowfall (>16 dBZ) occurs 10% of the time, and a large fraction of cloud
475 profiles have very low reflectivity (producing little or no precipitation), consistent with the open-
476 cellular appearance on satellite imagery (Fig. 1). The surface temperature is almost always below
477 4°C during CAOs (Fig. 10b), so the melting layer is generally below 400 m MSL. Therefore,
478 snow, not rain, dominates the first level with KAZR data (200 m MSL) and all levels above
479 during CAOs. The spread in Doppler velocities is large, with hydrometeors carried up ~11% of
480 the time. Spectral widths vary considerably, with >10% of the profiles experiencing values over
481 0.5 m s^{-1}.
482 WAI clouds are more frequently deep. The color scheme of the frequency differences in
483 the right panels in Fig. 12 matches that of previous figures: red indicates higher frequencies
484 during WAIs. WAI clouds are far more homogenous and continuous compared to CAO clouds,
485 and are generally precipitating: only ~10% of the profiles have low-level reflectivity values
486 below -20 dBZ. Hydrometeors almost all fall, at a speed increasing towards the surface,
487 indicating stratiform snow growth with ice particles growing mostly by vapor diffusion on their

488 way down [Section 6.3 in Houze (2014)]. The spectral width distribution above the melting layer
489 is narrow compared to CAO clouds. The melting level indicated by rapidly increasing spectral
490 width and fall speed is typically below 1.5 km MSL during WAIs.
491
492 **5. Discussion**
493 The vertical structure of clouds and precipitation are quite different during the yin and
494 yang of Arctic-midlatitude heat exchange, i.e. marine CAOs and WAIs, as seen from the
495 perspective of a coastal site in northern Norway. Clouds in WAIs are stratiform, driven by large-
496 scale ascent. The high PWV in strong southwesterly flow and deep, ice-dominant clouds lead to
497 persistent precipitation. At times, the WAI cloud regime is shallow, with relatively warm cloud
498 tops. Driven by oceanic surface heat fluxes over a fetch of 1,000-1,300 km, clouds in marine
499 CAOs are mostly convective and relatively shallow. They produce significant, but intermittent,
500 precipitation at all distances from the Arctic ice edge, with open cells producing moderate snow
501 showers at Andenes. The spectrum of marine CAO cloud properties is rather continuous (Fig.
502 10), but two cloud modes can be distinguished, and they have distinct environmental conditions.
503 One mode, illustrated herein (the 13 March 2020 case, Section 3a), is characterized by pockets of
504 strong updrafts and convective turbulence, alternating with decaying convective cells and
505 occasionally high reflectivity with heavy surface precipitation rate (Fig. 6 and 7). This CAO
506 mode, referred to as the open-cell mode, has cloud tops ranging between 2 and 5 km MSL,
507 pockets of high IWP, occasionally high LWP, and broken cloud cover (Fig. 6). This mode tends
508 to occur in an environment with high M values and/or strong surface winds. A second mode,
509 referred to as the closed-cell mode, typically is associated with lower cloud tops (mostly between
510 2-3 km), mostly continuous cloud cover but low reflectivity values. The vertical air drafts,
511 turbulence, LWP, and precipitation rate are relatively benign. This closed-cell mode is far less
512 common (~10% of CAO periods in COMBLE) and tends to occur under low M values, and
513 weaker surface winds. The contrast between the open- and closed-cell modes and their
514 controlling environmental factors are being explored further.
515 One limitation of this study is that it only examines CAOs and WAIs cloud vertical
516 structure at one coastal site (Andenes) and not at other longitudes around 70°N. In winter, the
517 far-northern Atlantic is the main pathway for WAIs into the Arctic (Woods et al. 2013), but
518 marine CAOs are frequently found elsewhere, especially off the boreal continents (Fletcher et al.

519 2016). Our 6-month Andenes-centric CAO "climatology" excludes the relatively weak and short-
520 lived CAOs originating in the Fram Strait that do not reach Andenes due to the long distance
521 from the ice-edge. It also excludes CAOs emerging from the northeast (the Barents Sea) that
522 affect the Norwegian Sea north of Andenes or the northern tip of Scandinavia but leave Andenes
523 (on the NW side, Fig. 1) somewhat sheltered by the terrain. Both types of CAOs occurred during
524 COMBLE. Thus, not the whole spectrum of CAOs over the Norwegian Sea is captured by our
525 Andenes-centric climatology, and observation at Andenes might skew towards intense CAOs
526 originating in the Fram Strait.
527 For WAIs identified at Andenes, the most impacted areas were the Norwegian Sea, the
528 Norwegian coast, but also the eastern coast of Greenland, and sea ice east of the Greenland coast.
529 The reason for this eastward extent is that the moist, warm air sometimes wrapped around the
530 Icelandic low towards Greenland, as was the case on 4 December 2019 (Fig. 4). At later times,
531 the WAIs observed during COMBLE often impacted areas further northeast, mainly in the
532 Barents Sea. The WAIs in our study rarely transported high temperatures and moisture deep into
533 the central Arctic, unlike events described by Woods et al. (2013) (1-3 Jan 1998) and by Dada et
534 al. (2022) (mid-April 2020). Nevertheless, the cloud vertical structure of WAIs described herein
535 is likely representative for those WAIs that do penetrate deep in the central Arctic.
536
537 **6. Conclusion**
538 This study uses data from profiling in situ and remote sensors that were deployed during
539 COMBLE between 1 December 2019 and 31 May 2020 at a coastal site in northern Norway
540 (69.1°N), to characterize high-latitude marine CAOs and WAIs. This site is suitably located to
541 capture major WAIs into the Arctic, and also frequently witnesses the CAO cloud regime that
542 forms when air masses are advected from the Arctic sea ice over some 1000 km of open water.
543 CAOs are objectively defined in terms of low-level thermal instability relative to the sea surface
544 temperature, and WAIs in terms of low-level stratification of moist static energy. The main
545 conclusions are as follows:
546 • Cloud structures in CAOs are convective, driven by strong surface heat fluxes as Arctic air
547 masses are advected over a long fetch of open water. The mostly stratiform clouds and
548 precipitation in WAIs into the Arctic are the result of synoptically ascending currents
549 containing and transporting much water vapor.

- At Andenes, the CAO cloud regime is dominated by an open-cellular structure with cloud tops mostly between 2-5 km. The cumulus clouds are generally precipitating, and intense CAOs may produce showers containing much ice and producing moderate precipitation. Depending on the lifecycle stage of convective cells, they may contain substantial liquid water as well.
- A variety of cloud top heights and cloud depths occur at Andenes during WAIs, and sometimes cloud layering occurs with one or more interspersed dry layers. The WAI cloud regime is marked by high PWV and LWP values, but relatively little IWP and higher precipitation rates compared to CAO clouds.

Future COMBLE-based work will further characterize the CAO cloud regime, in particular the mesoscale organization, the vertical structure, radiative fluxes, relations between microphysical and dynamical properties, and precipitation growth mechanism, using observations and high-resolution numerical simulations.

Acknowledgements: The COMBLE campaign was enabled by an ARM Mobile Facility deployment proposal to the Office of Science of the U.S. Dept. of Energy (DOE). This research was supported by DOE Atmospheric Systems Research (ASR) grants DE-SC0018927 and DE-SC0021151.

Data Availability Statement: COMBLE campaign data at the Andenes site (ANX) are available at https://adc.arm.gov/discovery/#/results/site_code::anx. C-band radar reflectivity is obtained from https://thredds.met.no/thredds/catalog/remotesensing/reflectivity-nordic/catalog.html. Satellite images herein were created using VIIRS/NPP Imagery Resolution 6-Min L1B Swath 375m (https://doi.org/10.5067/VIIRS/VNP02IMG.002), VIIRS/NPP Imagery Resolution Terrain-Corrected Geolocation 6-Min L1 Swath 375m (https://doi.org/10.5067/VIIRS/VNP03IMG.002), VIIRS/JPSS1 Imagery Resolution 6-Min L1B Swath 375m (https://doi.org/10.5067/VIIRS/VJ102IMG.021) , and VIIRS/JPSS1 Imagery Resolution Terrain-Corrected Geolocation 6-Min L1 Swath 375m (https://doi.org/10.5067/VIIRS/VJ103IMG.021). The NOAA Air Resources Laboratory provides HYSPLIT at https://www.ready.noaa.gov/HYSPLIT.php, which was used to create trajectories.

This study uses ERA5 hourly data at the surface (https://doi.org/10.24381/cds.adbb2d47) and at constant pressure levels (https://doi.org/10.24381/cds.bd0915c6), in addition to monthly average data on constant pressure levels (https://doi.org/10.24381/cds.6860a573). The NOAA Optimum Interpolation ¼ Degree Daily Sea Surface Temperature (OISST) Analysis, Version 2.1 is available at https://doi.org/10.7289/V5SQ8XB5.

References

Aemisegger, F., & L. Papritz (2018). A Climatology of Strong Large-Scale Ocean Evaporation Events. Part I: Identification, Global Distribution, and Associated Climate Conditions. *J. Climate*, 31, 7287–7312. https://doi.org/10.1175/JCLI-D-17-0591.1

Aikins, J., K. Friedrich, B. Geerts and B. Pokharel (2016). Role of a low-level jet and turbulence on winter orographic snowfall. *Mon. Wea. Rev*., 144, 3277–3300. http://dx.doi.org/10.1175/MWR-D-16-0025.1

Burk, K. (2019). Balloon-Borne Sounding System (SONDEWNPN). Atmospheric Radiation Measurement (ARM) User Facility. https://doi.org/10.5439/1595321

Cromwell, E., & Bartholomew, M. (2019). Weighing Bucket Precipitation Gauge (WBPLUVIO2). Atmospheric Radiation Measurement (ARM) User Facility. https://doi.org/10.5439/1338194

Dada, L., Angot, H., Beck I., Baccarini, A., Quéléver, L. L. J., Boyer, M., et al. (2022). A central arctic extreme aerosol event triggered by a warm air-mass intrusion. *Nat. Commun.* 13, 5290. https://doi.org/10.1038/s41467-022-32872-2

Davy, R., & Outten, S. (2020). The Arctic Surface Climate in CMIP6: Status and Developments since CMIP5, *Journal of Climate*, 33(18), 8047-8068. https://doi.org/10.1175/JCLI-D-19-0990.1

Dahlke, S., Solbès, A., & Maturilli, M. (2022). Cold air outbreaks in Fram Strait: Climatology, trends, and observations during an extreme season in 2020. *Journal of Geophysical Research: Atmospheres*, 127, e2021JD035741. https://doi.org/10.1029/2021JD035741

Dickson, R.R., Lazier, J., Meincke, J., Rhines, P., & Swift, J. (1996). Long-term coordinated changes in the convective activity of the North Atlantic. *Prog. Oceanogr*. 38: 241–295. https://doi.org/10.1016/S0079-6611(97)00002-5

611 Doyle, J. G., Lesins, G., Thackray, C. P., Perro, C., Nott, G. J., Duck, T. J., et al. (2011). Water
612 vapor intrusions into the High Arctic during winter, *Geophys. Res. Lett.*, 38, L12806.
613 https://doi.org/10.1029/2011GL047493
614 Fan, Q., Xu, X., He, S., & Zhou, B. (2022): The extreme Arctic warm anomaly in November
615 2020, *Atmospheric and Oceanic Science Letters*, 15.
616 https://doi.org/10.1016/j.aosl.2022.100260
617 Fletcher, J. K., Mason, S. L., & Jakob, C. (2016). The climatology, meteorology, and boundary
618 layer structure of marine cold air outbreaks in both hemispheres. *J. Climate*, 29, 1999–2014.
619 https://doi.org/10.1175/JCLI-D-15-0268.1
620 Geerts, B., Giangrande, S. E., McFarquhar, G. M., Xue, L. Abel, S. J., Comstock, J. M., et al.
621 (2022). The COMBLE campaign: a study of marine boundary-layer clouds in Arctic cold-air
622 outbreaks. *Bulletin of the American Meteorological Society.* https://doi.org/10.1175/BAMS-
623 D-21-0044.1
624 Grasmick, C., Geerts, B., French, J., Haimov, S., & Rauber, R. M. (2022). Estimating
625 microphysics properties in ice-dominated clouds from airborne Ka – W band dual-
626 wavelength ratio reflectivity in close proximity to in situ probes. *J. Atmos. Oceanic Technol.*.
627 https://doi.org/10.1175/JTECH-D-21-0147.1
628 Guan, B., & Waliser , D. E. (2015). Detection of atmospheric rivers: Evaluation and application
629 of an algorithm for global studies. *J. Geophys. Res. Atmos.*, **120**, 12 514–12 535.
630 https://doi.org/10.1002/2015JD024257
631 Hardin, J., Hunzinger, A., Schuman, E., Matthews, A., Bharadwaj, N., Varble, A., et al. (2019).
632 Ka ARM Zenith Radar (KAZRCFRGEQC). Atmospheric Radiation Measurement (ARM)
633 User Facility. https://doi.org/10.5439/1615726
634 Hersbach, H., Bell, B., Berrisford, P., Hirahara, S., Horányi, A., Muñoz-Sabater, J., et al. (2020).
635 The ERA5 global reanalysis. *Quarterly Journal of the Royal Meteorological Society*,
636 146(730), 1999-2049. https://doi.org/10.1002/qj.3803
637 Houze Jr, R. A. (2014). *Cloud dynamics*. Second Edition. Academic press, 432 pp.
638 Hu, Y, Geerts, B., Deng, M., Grasmick, C., Wang, Y., Lackner, C. P., et al. (2022). Vertical
639 structure and ice production processes of shallow convective post-frontal clouds over the
640 Southern Ocean in MARCUS, Part I: Observational study. *J. Atmos. Sci.*, in review.

Jensen, M., Giangrande, S., Fairless, T., & Zhou, A. (2019). Interpolated Sonde (INTERPOLATEDSONDE). Atmospheric Radiation Measurement (ARM) User Facility. https://doi.org/10.5439/1095316

Johnson, K., Giangrande, S., & Toto, T. (2019). Active Remote Sensing of Clouds (ARSCL) product using Ka-band ARM Zenith Radars (ARSCLKAZRBND1KOLLIAS). Atmospheric Radiation Measurement (ARM) User Facility. https://doi.org/10.5439/1393438

Keeler, E., Kyrouac, J., & Ermold, B. (2019). Automatic Weather Station (MAWS). Atmospheric Radiation Measurement (ARM) User Facility. https://doi.org/10.5439/1182027

Kim, BM., Hong, JY., Jun, SY. *Et al.* (2017). Major cause of unprecedented Arctic warming in January 2016: Critical role of an Atlantic windstorm. *Sci Rep* **7**, 40051. https://doi.org/10.1038/srep40051

Kolstad, E. W., & Bracegirdle, T. J. (2008). Marine cold-air outbreaks in the future: An assessment of IPCC AR4 model results for the Northern Hemisphere. *Climate Dyn*., **30**, 871–885. https://doi.org/10.1007/s00382-007-0331-0

Kulie, M. S., Milani, L., Wood, N. B., Tushaus, S. A., Bennartz, R., & L'Ecuyer, T. S. (2016). A shallow cumuliform snowfall census using spaceborne radar. *Journal of Hydrometeorology*, 17(4), 1261-1279. https://doi.org/10.1175/JHM-D-15-0123.1

Kulie, M. S., & Milani, L., (2018). Seasonal variability of shallow cumuliform snowfall: A Cloud-Sat perspective. *Quarterly Journal of the Royal Meteorological Society*; 144 (Suppl. 1): 329– 343. https://doi.org/10.1002/qj.3222

Kyrouac, J., & Shi, Y. (2019). Surface Meteorological Instrumentation (MET). Atmospheric Radiation Measurement (ARM) User Facility. https://doi.org/10.5439/1786358

Mages, Z., Kollias, P., Zhu, Z., & Luke, E. P., (2022). Surface-based observations of cold-air outbreak clouds during the COMBLE field campaign, *Atmos. Chem. Phys. Discuss*. [preprint], https://doi.org/10.5194/acp-2022-546 , in review.

Mateling, M. E., Pettersen, C., Kulie, M. S., & L'Ecuyer, T. S. (2022). Marine Cold-Air Outbreak Snowfall in the North Atlantic: A CloudSat Perspective. *JGR Atmospheres*, in review.

Milani, L., Kulie, M. S., Casella, D., Kirstetter, P. E., Panegrossi, G., Petkovic, V., et al. (2021). Extreme Lake-Effect Snow from a GPM Microwave Imager Perspective: Observational

671 Analysis and Precipitation Retrieval Evaluation, *Journal of Atmospheric and Oceanic*
672 *Technology*, *38*(2), 293-311. https://doi.org/10.1175/JTECH-D-20-0064.1
673 Miller, M. A., Nitschke, K., Ackerman, T. P., Ferrell, W. R., Hickmon, N., & Ivey, M., (2016).
674 The ARM Mobile Facilities, *Meteorol. Monogr.*, **57**, 9.1–9.15.
675 https://doi.org/10.1175/AMSMONOGRAPHS-D-15-0051.1
676 Minder, J. R., D. R. Durran, G. H. Roe, and A. Anders (2008). The climatology of small-scale
677 orographic precipitation over the Olympic Mountains: Patterns and processes. *Quart. J. Roy.*
678 *Meteor. Soc.*, 134, 817–839, https://doi.org/10.1002/qj.258
679 Naud, C. M., Booth, J. F., Lamer, K., Marchand, R., Protat, A., & McFarquhar, G. M. (2020). On
680 the relationship between the marine cold air outbreak M parameter and low-level cloud
681 heights in the midlatitudes. *Journal of Geophysical Research: Atmospheres*, 125,
682 e2020JD032465. https://doi.org/10.1029/2020JD032465
683 Oltmanns, M., Straneo, F., & Tedesco, M. (2019). Increased Greenland melt triggered by large-
684 scale, year-round cyclonic moisture intrusions. *The Cryosphere*, 13, 815–825.
685 https://doi.org/10.5194/tc-13-815-2019
686 Papritz, L., & Grams, C. M. (2018). Linking low-frequency large-scale circulation patterns to
687 cold air outbreak formation in the northeastern North Atlantic. *Geophysical Research Letters*,
688 45(5), 2542-2553. https://doi.org/10.1002/2017GL076921
689 Papritz, L., & Sodemann, H. (2018). Characterizing the Local and Intense Water Cycle during a
690 Cold Air Outbreak in the Nordic Seas, *Monthly Weather Review*, *146*(11), 3567-3588.
691 https://doi.org/10.1175/MWR-D-18-0172.1
692 Pithan, F., & Mauritsen, T. (2014). Arctic amplification dominated by temperature feedbacks in
693 contemporary climate models. *Nature Geosci.*, 7, 181-184. https://doi.org/10.1038/ngeo2071
694 Pithan, F., Svensson, G., Caballero, R., Chechin, D., Cronin, T. W., Ekman, A. M. L., et al.
695 (2018). Role of air-mass transformations in exchange between the Arctic and mid-latitudes.
696 *Nature Geosci* **11,** 805–812. https://doi.org/10.1038/s41561-018-0234-1
697 Ralph, F. M., Iacobellis, S. F., Neiman, P. J., Cordeira, J. M., Spackman, J. R., Waliser, D. E., et
698 al.(2017). Dropsonde observations of total water vapor transport within North Pacific
699 atmospheric rivers. *J. Hydrometeor.*, **18**, 2577–2596. https://doi.org/10.1175/JHM-D-17-
700 0036.1

Renfrew, I. A., & Moore, G. W. K. (1999). An extreme cold-air outbreak over the Labrador Sea: Roll vortices and air–sea interaction. *Monthly Weather Review*, 127(10), 2379-2394. https://doi.org/10.1175/1520-0493(1999)127<2379:AECAOO>2.0.CO;2

Reynolds, R. W., Banzon, V. F., & NOAA CDR Program (2008). NOAA Optimum Interpolation 1/4 Degree Daily Sea Surface Temperature (OISST) Analysis, Version 2. *NOAA National Centers for Environmental Information*. https://doi.org/10.7289/V5SQ8XB5

Rolph, G., Stein, A., & Stunder, B., (2017). Real-time Environmental Applications and Display sYstem: READY. *Environmental Modelling & Software*, 95, 210-228. https://doi.org/10.1016/j.envsoft.2017.06.025

Ruiz-Donoso, E., Ehrlich, A., Schäfer, M., Jäkel, E., Schemann, V., Crewell, S., et al. (2020). Small-scale structure of thermodynamic phase in Arctic mixed-phase clouds observed by airborne remote sensing during a cold air outbreak and a warm air advection event, *Atmos. Chem. Phys.*, 20, 5487–5511. https://doi.org/10.5194/acp-20-5487-2020

Rutz. J. J., Guan, B., Bozkurt, D., Gorodetskaya, I. V., Gershunov, A., Lavers, D. A., et al. (2020). Global and Regional Perspectives. In: Ralph, F., Dettinger, M., Rutz, J., Waliser, D. (eds) *Atmospheric Rivers*. Springer, Cham. https://doi.org/10.1007/978-3-030-28906-5_4

Saltikoff, E., Kurri, M., Leijnse, H., Barbosa, S., & Stiansen, K. (2017). Maintenance Keeps Radars Running, *Bulletin of the American Meteorological Society*, 98(9), 1833-1840. https://doi.org/10.1175/BAMS-D-16-0095.1

Serreze, M. C., Barrett, A. P., Stroeve, J. C., Kindig, D. N., & Holland, M. M. (2009). The emergence of surface-based Arctic amplification, *Cryosphere*, 3, 11–19. https://doi.org/10.5194/tc-3-11-2009

Thoman, R. L., Druckenmiller, M. L., Moon, T. A., Andreassen, L. M., Baker, E., Ballinger, T. J., et al. (2022). State of the Climate in 2021 The Arctic. *Bull. Amer. Meteor. Soc.*, 103 (8), S257–S306. https://doi.org/10.1175/BAMS-D-22-0082.1

Tornow, F., Ackerman, A. S., & Fridlind, A. M. (2021), Preconditioning of overcast-to-broken cloud transitions by riming in marine cold air outbreaks, *Atmos. Chem. Phys.*, 21, 12049–12067. https://doi.org/10.5194/acp-21-12049-2021

Wang, M., Giangrande, S., Johnson, K., & Jensen, M. (2019). improved MICROBASE product with Uncertainties (MICROBASEKAPLUS). Atmospheric Radiation Measurement (ARM) User Facility. https://doi.org/10.5439/1768890

Wendisch, M.,Handorf, D.,Tegen, I.,Neggers, R. A. J., & Spreen, G. (2021). Glimpsing the ins and outs of the Arctic atmospheric cauldron, *Eos, 102.* https://doi.org/10.1029/2021EO155959. Published on 16 March 2021.

West, T. K., Steenburgh, W. J., & Mace, G. G. (2019). Characteristics of sea-effect clouds and precipitation over the sea of Japan region as observed by A-Train satellites. *Journal of Geophysical Research: Atmospheres*, 124(3), 1322-1335. https://doi.org/10.1029/2018JD029586

Woods, C., Caballero, R., & Svensson, G. (2013). Large-scale circulation associated with moisture intrusions into the Arctic during winter. *Geophys. Res. Lett*.,40, 4717–4721. https://doi.org/10.1002/grl.50912

Woods, C., & Caballero, R. (2016). The role of moist intrusions in winter Arctic warming and sea ice decline. *J. Climate*, 29,4473–4485. https://doi.org/10.1175/JCLI-D-15-0773.1

Woods, C., Caballero, R., & Svensson, G. (2017). Representation of Arctic Moist Intrusions in CMIP5 Models and Implications for Winter Climate Biases, *Journal of Climate*, *30*(11), 4083-4102. https://doi.org/10.1175/JCLI-D-16-0710.1

Xiao, C., & Shaocheng, X. (2019). ARM Best Estimate Data Products (ARMBEATM). Atmospheric Radiation Measurement (ARM) User Facility. https://doi.org/10.5439/1333748

Yang, W., & Magnusdottir, G. (2017). Springtime extreme moisture transport into the Arctic and its impact on sea ice concentration, *J. Geophys. Res. Atmos.*, 122, 5316– 5329. https://doi.org/10.1002/2016JD026324

You, C., Tjernström, M., and Devasthale, A. (2022). Warm and moist air intrusions into the winter Arctic: a Lagrangian view on the near-surface energy budgets, *Atmos. Chem. Phys*., 22, 8037–8057, https://doi.org/10.5194/acp-22-8037-2022

Zhang, D. (2019). MWR Retrievals (MWRRET1LILJCLOU). Atmospheric Radiation Measurement (ARM) User Facility. https://doi.org/10.5439/1027369

759 **Table 1**: COMBLE AMF1 datasets used in this study.

ARM Data Product	Description	Variable	Units
MET (Kyrouac & Shi, 2019)	surface meteorological instrumentation	atmospheric temperature horizontal wind direction horizontal wind speed atmospheric pressure precipitation rate	°C ° m s^{-1} hPa mm hr^{-1}
MAWS (Keeler et al., 2019)	Vaisala automatic weather station	atmospheric temperature horizontal wind direction horizontal wind speed atmospheric pressure	°C ° m s^{-1} hPa
WBPLUVIO2 (Cromwell & Bartholomew, 2019)	Pluvio-2 Weighing Bucket Precipitation Gauge	precipitation	mm
ARMBEATM (Xiao & Shaocheng, 2019)	ARMBE: Atmospheric measurements	precipitation	mm hr^{-1}
KAZRCFRGEQC (Hardin et al., 2019)	Ka-Band ARM Zenith RADAR (KAZR); general mode, quality controlled	equivalent reflectivity factor mean Doppler velocity spectral width	dBZ m s^{-1} m s^{-1}
ARSCLKAZRBND1KOLLIAS (Johnson et al., 2019)	cloud boundaries retrieved from KAZRARSCL	cloud base height cloud top height	m m
MWRRET1LILJCLOU (Zhang, 2019)	microwave radiometer retrievals	liquid water path precipitable water vapor	kg m^{-2} kg m^{-2}
MICROBASEKAPLUS (Wang et al., 2019)	Microphysical retrievals	ice water content	kg m^{-3}
INTERPOLATEDSONDE (Jensen et al., 2019)	sounding data interpolated to 1 min	atmospheric pressure atmospheric moisture (RH) atmospheric temperature horizontal wind speed	hPa % °C m s^{-1}
SONDEWNPN (Burk, 2019)	6-hourly balloon-borne sounding data	atmospheric pressure dewpoint temperature atmospheric temperature horizontal wind speed	hPa °C °C m s^{-1}

760

761

762 **Table 2**: Average precipitation rate (mm hr^{-1}) and total precipitation (mm), for the CAO and WAI case studies,
763 and for all CAOs (Present Weather Detector) and WAIs (Pluvio-2 Weighing Bucket) in COMBLE. Gauge data
764 were continuous, except for the Present Weather Detector, which was not available 1.9% of the time during all
765 CAOs. Corresponding ERA5 data are shown in the last column.

	Precipitation	Gauge	ERA5
13-14 March CAO	*rate (mm hr^{-1})*	*0.22*	*0.25*
(27.6 hrs)	**total (mm)**	**6.1**	**7.3**
3-5 December WAI	*rate (mm hr^{-1})*	*0.85*	*0.66*
(48.5 hrs)	**total (mm)**	**41.4**	**32.1**
all CAOs	*rate (mm hr^{-1})*	*0.25*	*0.26*
(821 hrs)	**total (mm)**	**202.6**	**208.8**
all WAIs	*rate (mm hr^{-1})*	*0.32*	*0.32*
(766 hrs)	**total (mm)**	**245.8**	**246.9**

766
767
768 **Table 3**: Normalized frequency of occurrence of cloud layering, according to KAZR data.

	single cloud column	two cloud layers	three or more cloud layers	clear sky	missing data
CAO periods	59.5 %	24.4 %	10.3 %	5.0 %	0.8 %
WAI periods	46.5 %	31.1 %	16.9 %	4.5 %	1.0 %

769
770

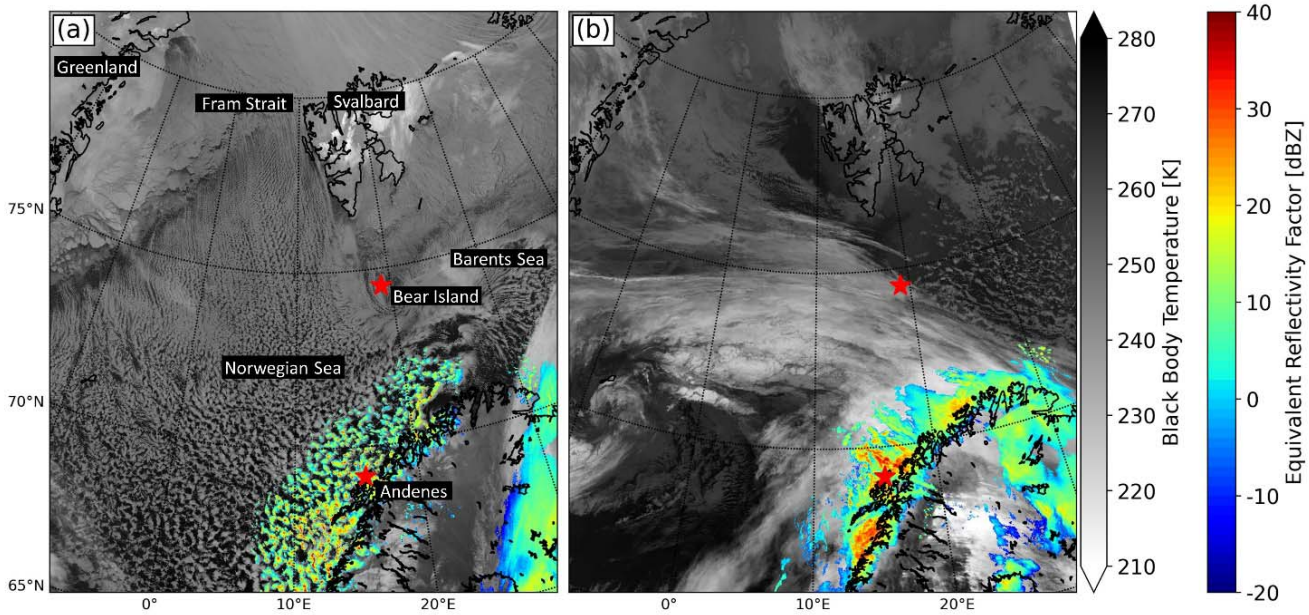

Fig. 1: Visible Infrared Imaging Radiometer Suite (VIIRS) I05 band (10.5 - 12.4 µm) image from (a) the NOAA-20 satellite and from (b) the Suomi NPP satellite, plus C-Band radar equivalent reflectivity factor from the Scandinavian composite of ground-based scanning radars. (a) CAO on 13 March 2020 at 11:18 UTC, with northerly flow off the ice edge, and (b) a WAI on 4 December 2019 at 11:42 UTC, with a moist plume in southwesterly flow off Scandinavia. The red stars mark the two COMBLE observational sites.

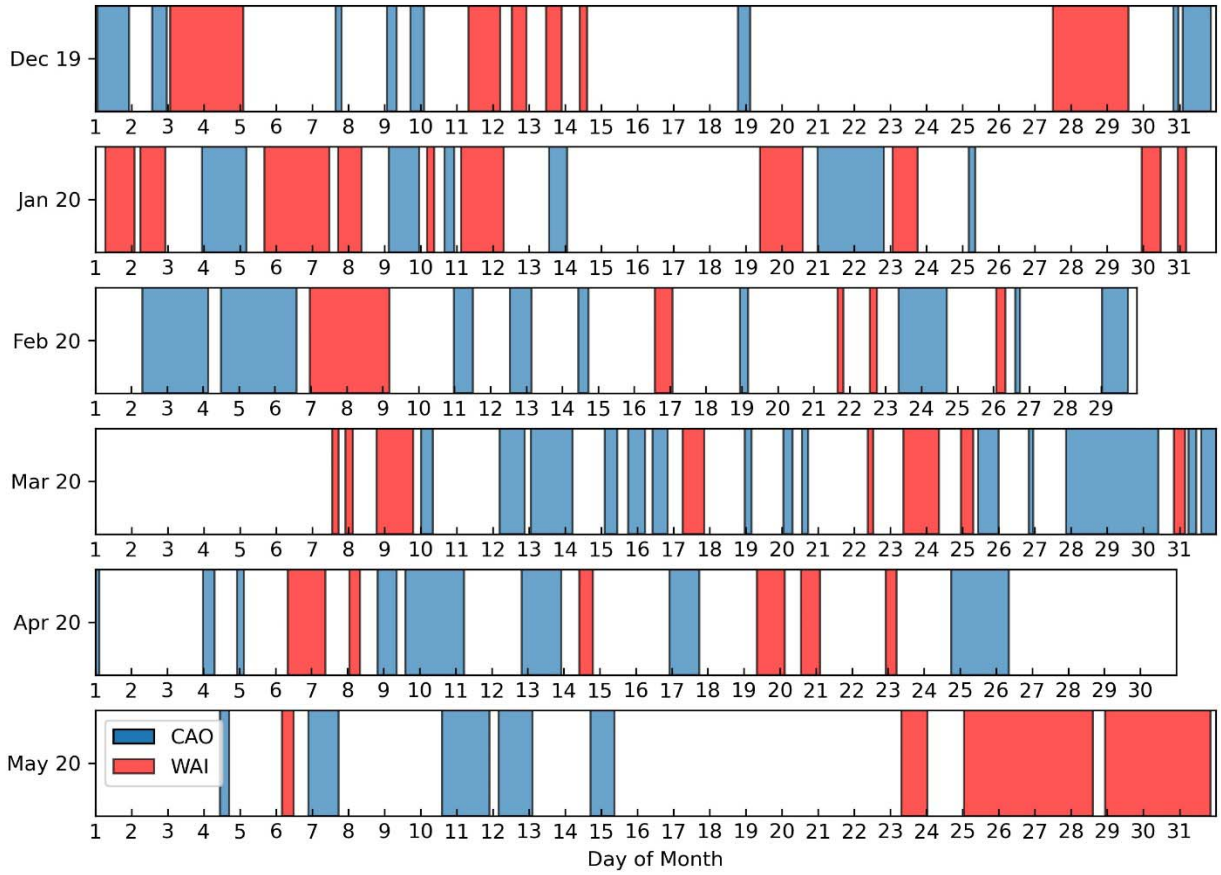

Fig. 2: Time periods of CAOs and WAIs at the AMF1 facility near Andenes during COMBLE, between 1 Dec 2019 and 31 May 2020.

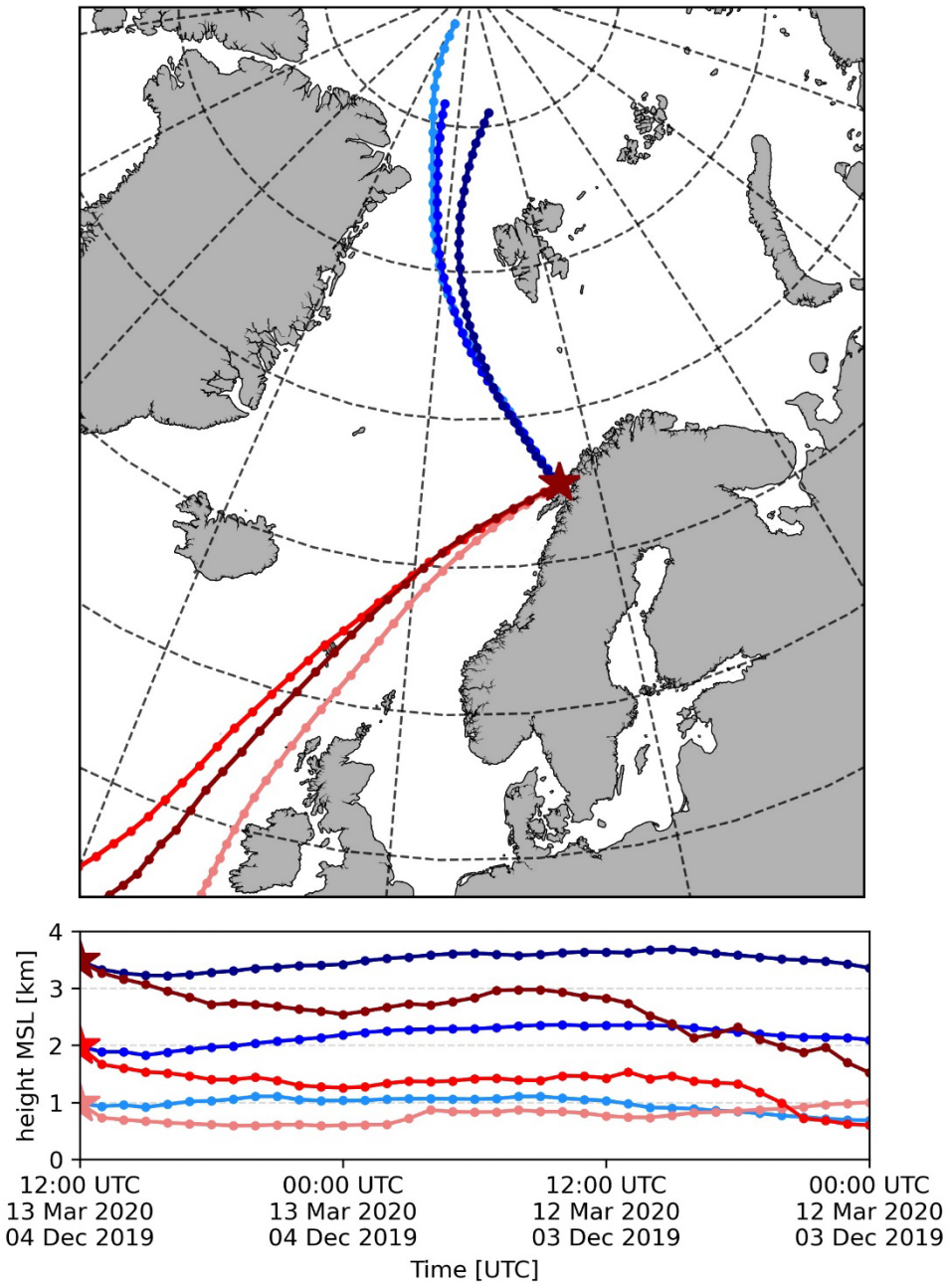

783
784 **Fig. 3**: Map and vertical profile of 36 hour back trajectories at multiple levels ending at Andenes (star) at 12
785 UTC on 13 March 2020 (CAO event; cold-colored trajectories) and at 12 UTC on 04 December 2019 (WAI
786 event; warm-colored trajectories) (data source: GFS model).
787

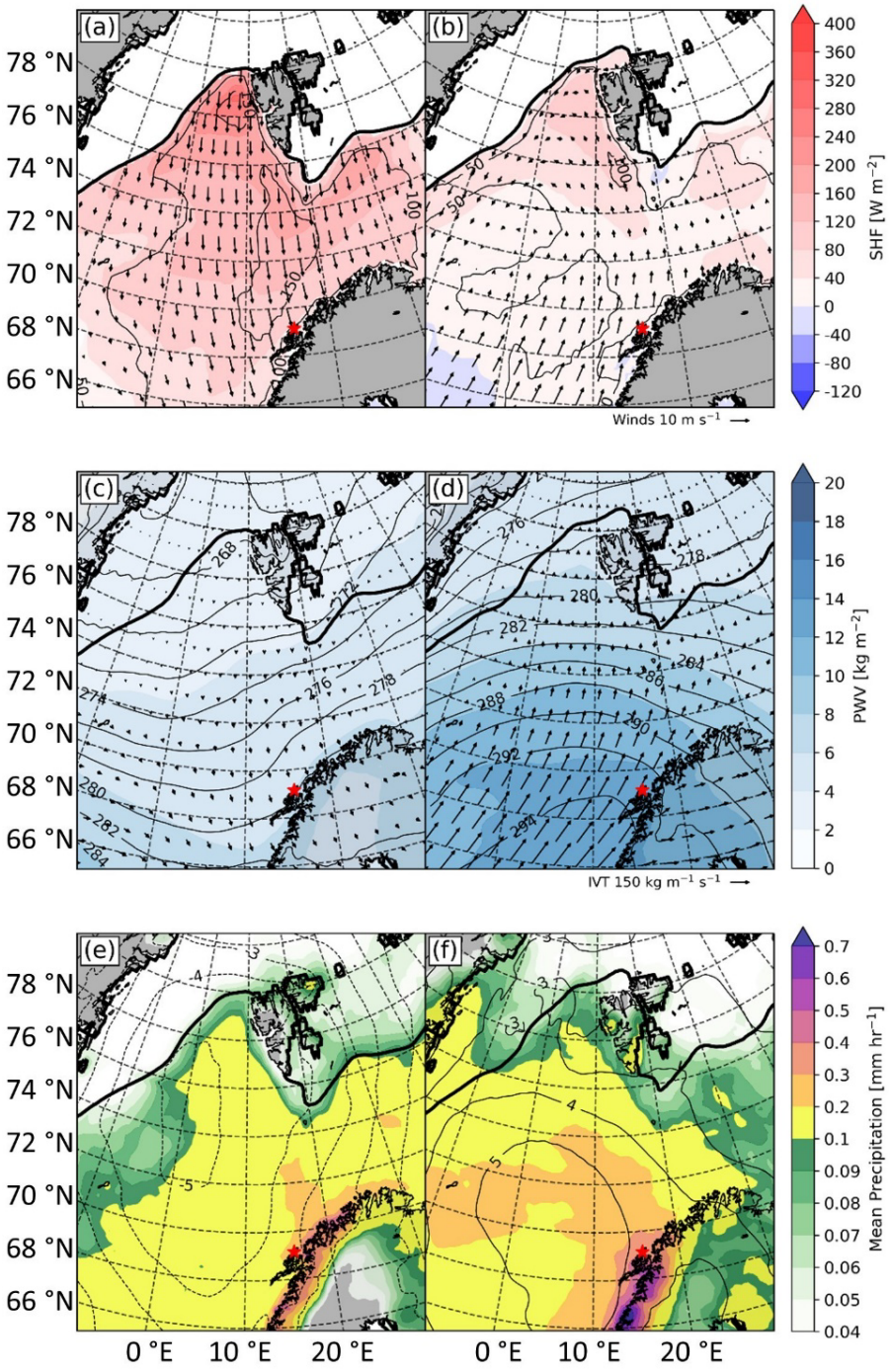

788

789 **Fig. 4**: Left column shows conditions for the CAO on 13 March 2020 at 12 UTC; right column shows
790 conditions for the WAI on 04 December 2019 at 12 UTC. (a) and (b) show surface sensible heat flux (color
791 fill), latent heat flux (contours, W m^{-2}), and 10 m winds (vectors) over open water. (c) and (d) show
792 precipitable water vapor PWV (color fill), 850 hPa θ_e(contours, K), and integrated vapor transport IVT
793 (vectors). (e) and (f) show the 850 hPa temperature anomaly (contours, K, dashed for negative values) at this
794 time, compared to the March 1991-2020 mean (e) and the December 1991-2020 mean (f). They also show the
795 average liquid-equivalent precipitation rate (color fill) for the duration of this CAO (e) and this WAI (f). The
796 bold black line is the sea ice edge (50% sea ice fraction) (data source: ERA5).

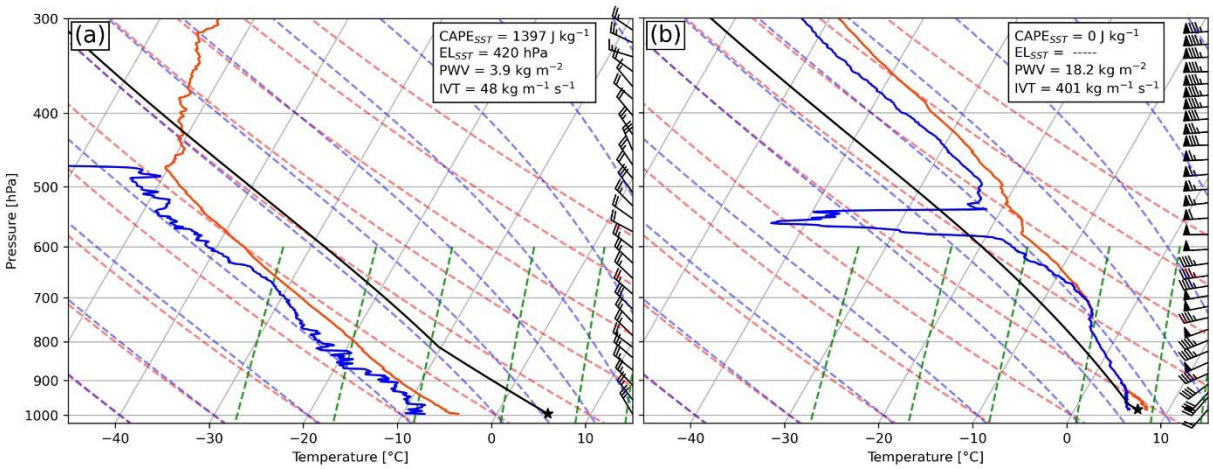

Fig. 5: Skew-T log-p and wind profile for (a) the CAO on 13 March 2020 at 11:26 UTC, and (b) the WAI on 04 December 2019 at11:27 UTC at Andenes. The bold black line indicates the ascent of a surface air parcel with a temperature equal to SST (marked with a star). Also listed are the CAPE and the equilibrium level (EL) for this parcel, as well as the PWV and IVT. A full barb equals 10 kts (data source: SONDEWNPN).

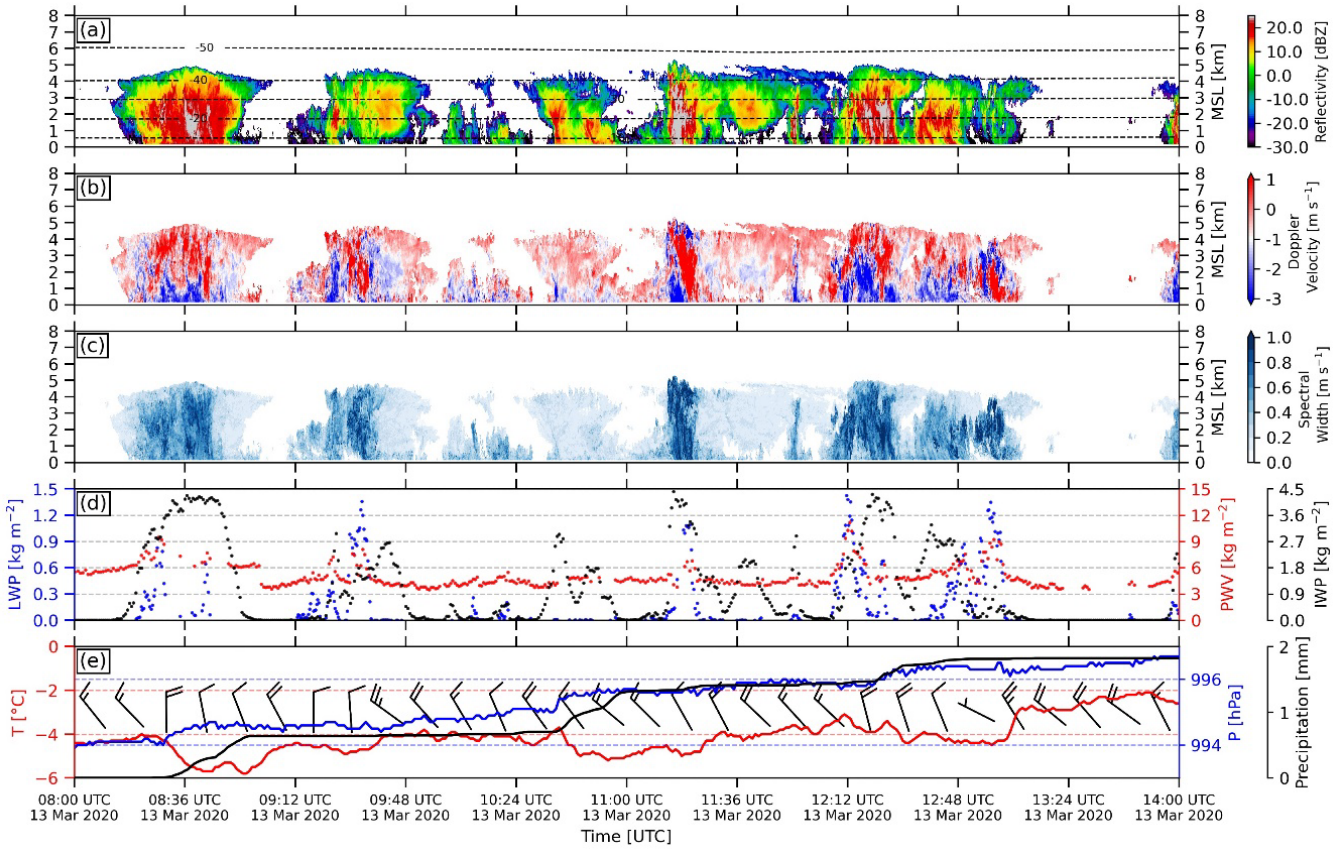

Fig. 6: A 6-hour time-height transect of (a) radar reflectivity, (b) Doppler Velocity, and (c) spectral width from KAZR; (d) LWP, PWV, and IWP; (e) surface air temperature, sea level pressure, cumulative gauge precipitation, and surface winds(barbs; every 18 minutes; full barb equals 10 kts), for the 13 March 2020 CAO. The dashed black lines in (a) are isotherms drawn at 10 °C intervals (data sources: see Table 1).

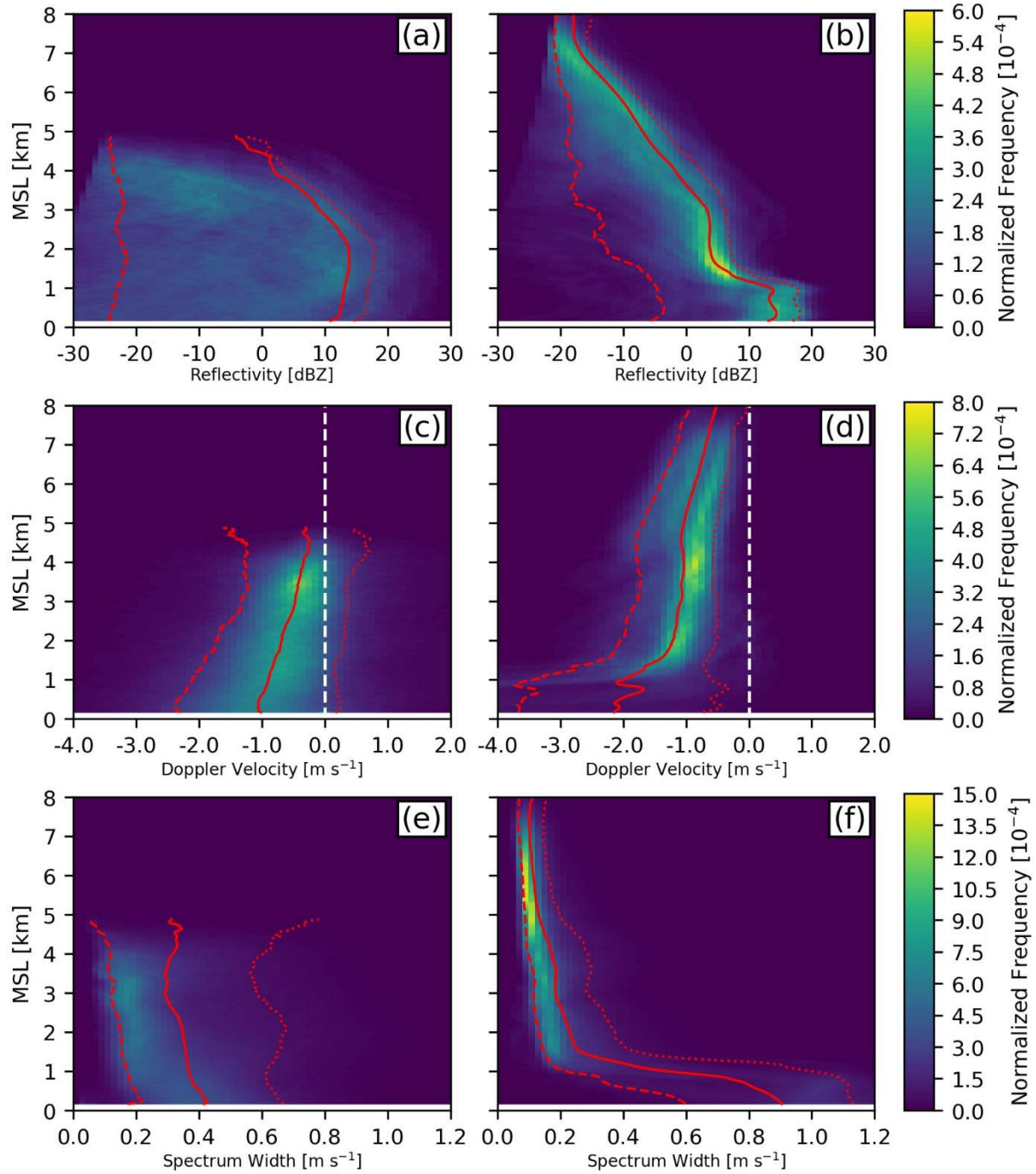

Fig. 7: Frequency by altitude display of KAZR (top) reflectivity, (middle) Doppler velocity, and (bottom) Doppler spectral width at Andenes, during the CAO (left panels), and the WAI (right panels). In each panel, from left to right, the red lines are the 10th percentile (dashed), the mean (solid), and the 90th percentile (dotted).

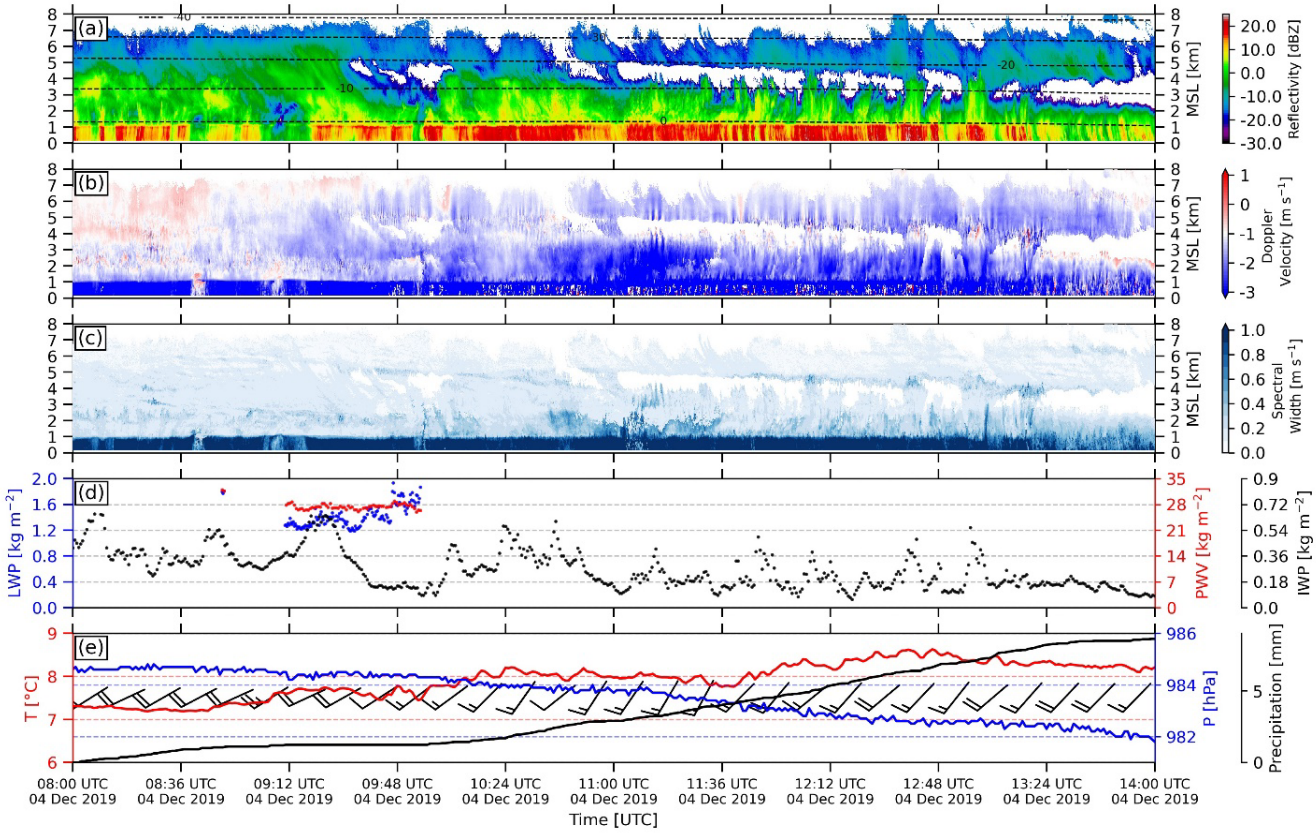

Fig. 8: As Fig. 6, but for a WAI period on 04 December 2019.

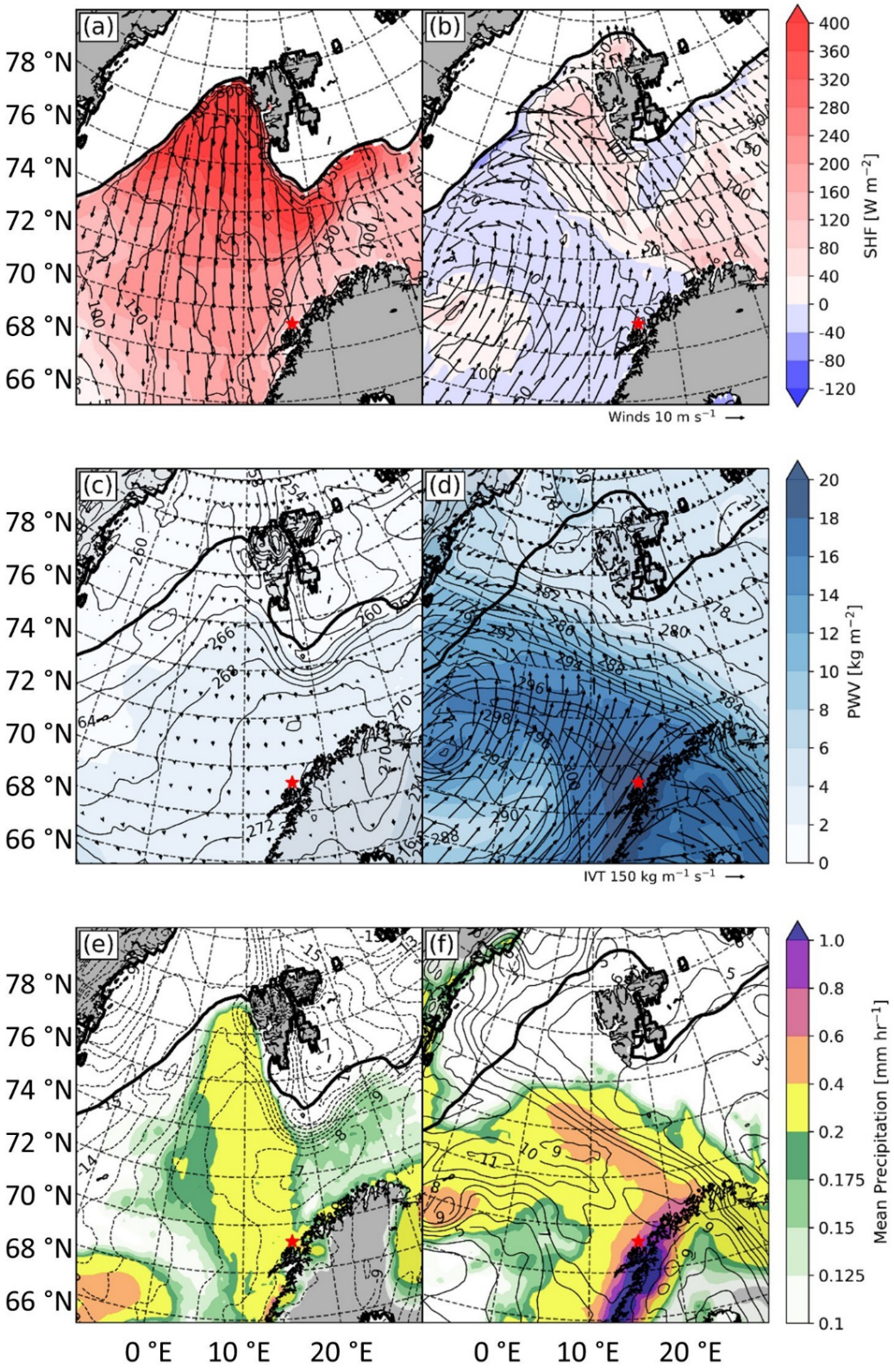

Fig. 9: As Fig. 4, but showing average conditions during all CAOs (left column) and all WAIs (right column). In (e) and (f), the temperature anomaly (contours) is the departure from the December to May 1991-2020 mean. The bold black line shows the average location of the sea ice edge (50 % sea ice fraction).

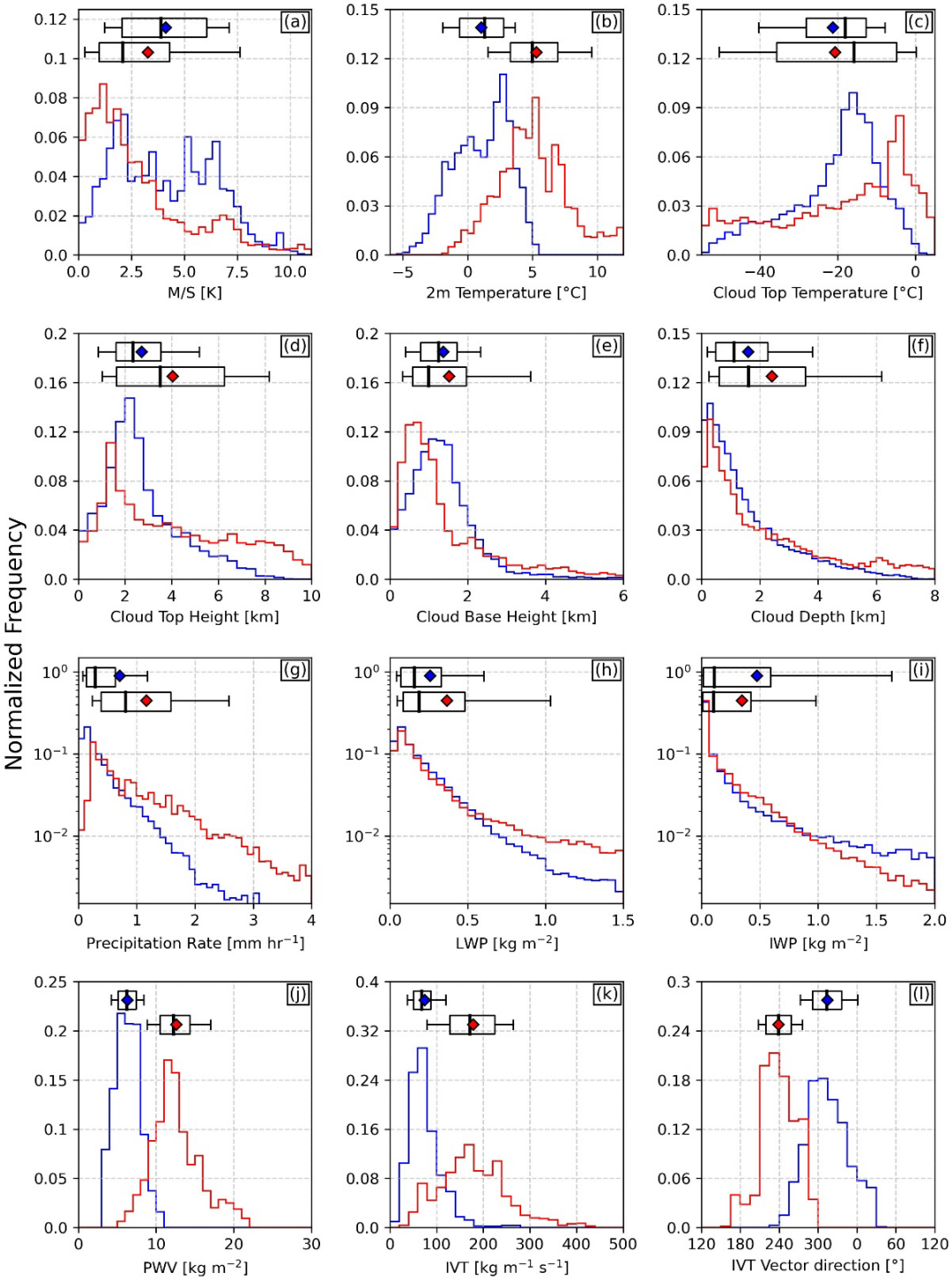

Fig. 10: Histograms of (a) *M* (*S*) values for CAOs (WAIs), (b) surface air temperature, (c) cloud top temperatures, (d) cloud top height, (e) cloud base height, (f) cloud depth, (g) 20-min average precipitation rate above 0.05 mm hr^{-1} (Pluvio-2 Weighing Bucket for WAI; Present Weather Detector for CAO), (h) LWP, (i) IWP, (j) PWV, (k) IVT, and (l) IVT vector direction (225° is from the SW, and 315° is from the NW) during all CAOs (blue) and all WAIs (red) at Andenes during COMBLE. Also shown for each distribution are the 10, 25, 50 (median), 75, and 90th percentiles (box with whiskers), plus the mean (blue/red diamond). Note that the ordinates in the middle row are logarithmic (data sources: see Table 1).

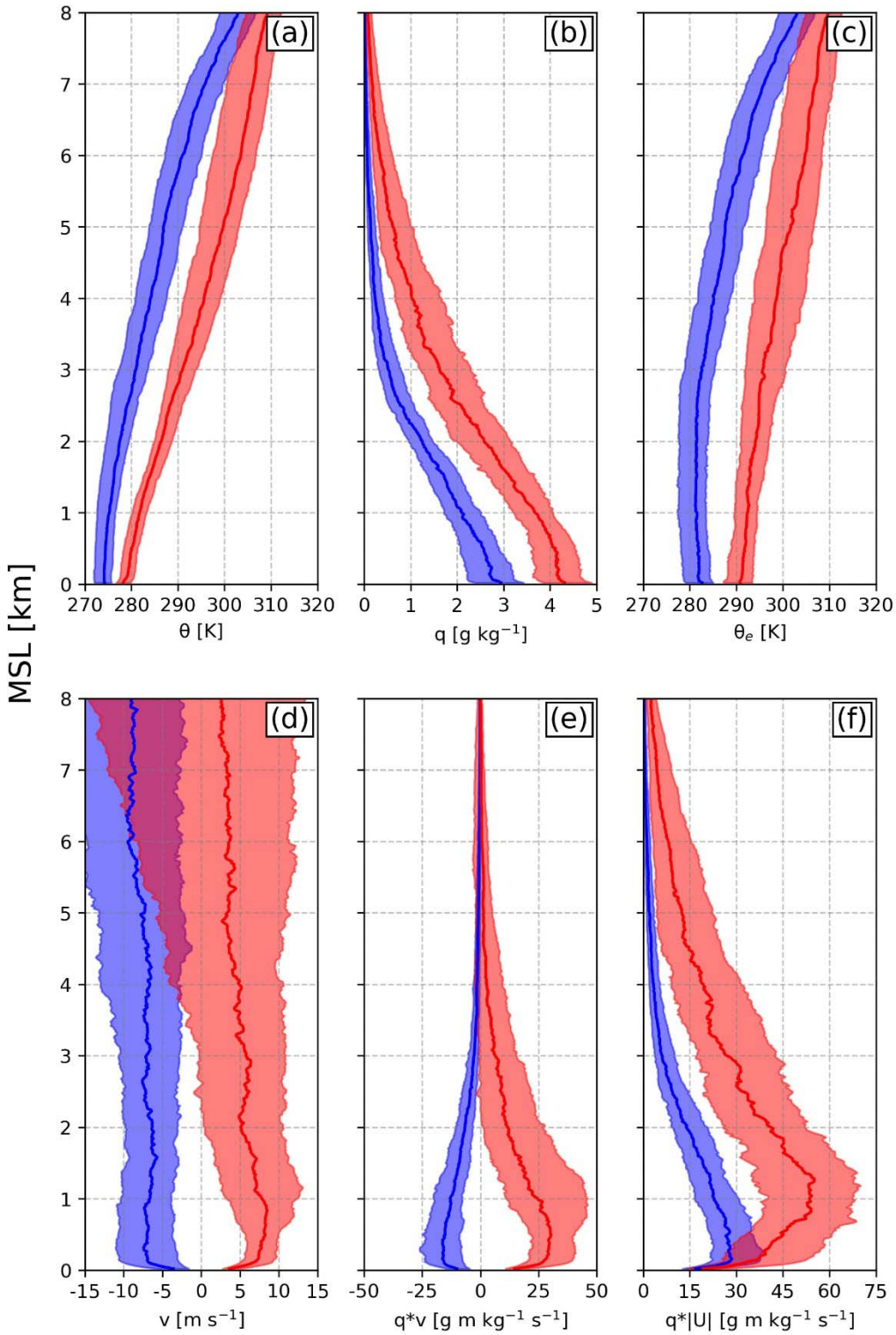

Fig. 11: Composite profiles of (a) potential temperature θ, (b) specific humidity q; (c) equivalent potential temperature θ_e; (d) meridional wind speed v; (e) meridional moisture transport qv; and (f) total moisture transport $q\vec{v}$. The blue (red) profiles represent the median for all CAOs (WAIs) in COMBLE, and the lighter shading around the median represent the 25th and 75th percentiles (data source: SONDEWNPN).

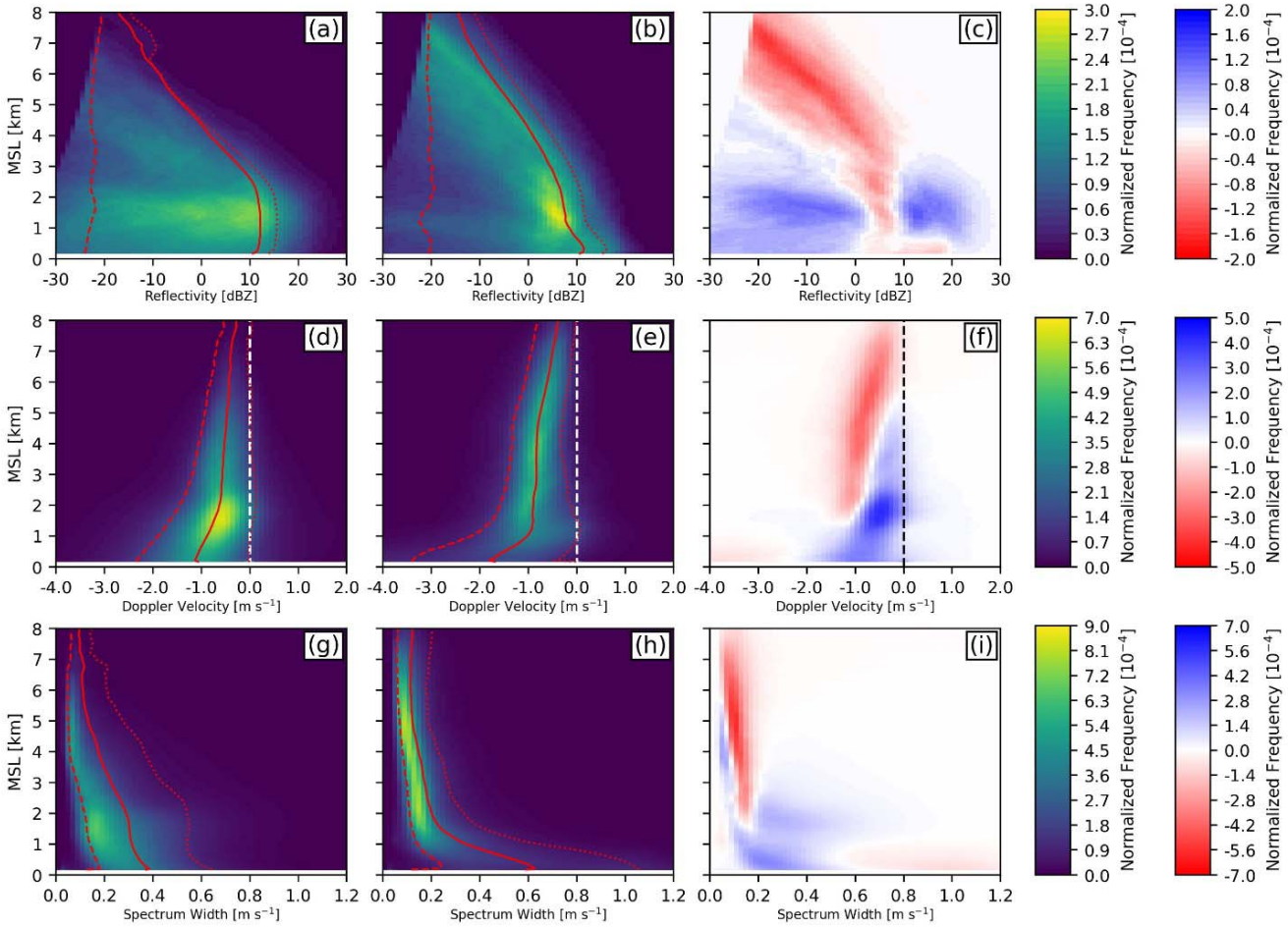

Fig. 12: Frequency by altitude display of KAZR (top) reflectivity, (middle) Doppler velocity, and (bottom) spectral width at Andenes, during (left panels) all CAO periods, (middle panels) all WAI periods, and (right panels) the difference [CAO-WAI], blue meaning more frequent during CAOs and red more frequent during WAIs. In each panel, from left to right, the red lines are the 10th percentile (dashed), the mean (solid), and the 90th percentile (dotted).